Geochimica et Cosmochimica Acta 427 (2026) 193–210

Contents lists available at ScienceDirect

Geochimica et Cosmochimica Acta

journal homepage: www.elsevier.com/locate/gca

Percolative core formation in oxidized planetesimals – I: experiments on melt migration in olivine aggregates

Varun Manilal [a,*], Kyusei Tsuno [a], Hideharu Kuwahara [b], Axel Wittmann [c], Anne Pommier [d], Christy Till [e], Damanveer S. Grewal [a,*]

[a] Department of Earth and Planetary Sciences, Yale University, New Haven, CT 06511, USA
[b] Geodynamics Research Center, Ehime University, Ehime 790-8577, Japan
[c] Eyring Materials Center, Arizona State University, Tempe, AZ 85281, USA
[d] Earth and Planets Laboratory, Carnegie Institution for Science, Washington, DC 20015, USA
[e] School of Earth and Space Exploration, Arizona State University, Tempe, AZ 85281, USA

ARTICLE INFO

Associate Editor: Bernard Charlier

Keywords:
Percolation
Core formation
High-pressure experiments
Dihedral angles
Carbonaceous chondrites

ABSTRACT

Percolation is a leading mechanism for metal-silicate segregation during the earliest stages of planetesimal differentiation triggered by ^{26}Al-heating. The efficacy of percolative core formation strongly depends on the compositions of metallic melts and co-existing silicate mineralogies. We report results from 21 high-pressure–temperature (P = 0.5–2 GPa; T = 1350 °C) experimental charges designed to simulate percolative core formation conditions in oxidized planetesimals. These experiments equilibrated olivine aggregates having variable FeO contents (0–30 wt%) with Fe-O-S metallic melts generated from two starting compositions (eutectic-like $Fe_{1.46}S$ and stoichiometric FeS). Our results quantify how pressure, FeO content in olivine, and metal composition affect oxygen solubility and dihedral angles in Fe-O-S alloys. Both O solubility and dihedral angles are largely insensitive to pressure over planetesimal conditions (P < 2 GPa) but are strongly dependent on olivine FeO content and metallic composition. For eutectic systems, dihedral angles decrease from 80° to 44° for olivine containing 1 wt% and 20 wt% FeO, respectively, crossing the critical interconnection threshold near 10 wt% FeO. For FeS systems, dihedral angles decrease more gradually (67° at 5 wt% FeO to 53° at 20 wt% FeO), consistent with the lower solubility of O in FeS-rich melts and a higher FeO threshold for connectivity. We developed a Langmuir competitive adsorption framework to explain these observations: S and O compete for interfacial binding sites at the olivine-metal boundary, with their relative coverage controlled by the activities of FeO and FeS. This predictive framework explains why O solubility is systematically lower in FeS-rich melts than in eutectic melts at the same fO_2 and demonstrates that both S and O act synergistically as surface-active elements that reduce dihedral angles and interfacial energies, with O exerting a stronger effect.

Applying these results to differentiation of oxidized planetesimals (fO_2 > IW; based on the compositions of oxidized chondrites), we find that the first-formed metallic melts would have formed interconnected networks at extremely low melt fractions and were capable of forming cores prior to widespread silicate melting in their parent bodies. Using the experimentally defined connectivity and O-solubility thresholds, we model core compositions in oxidized planetesimals as combinations of eutectic and FeS-rich Fe-O-S melts. The resulting metallic cores are predicted to be consistently O-bearing, ranging from ~3–4 wt% O in CM-/CI-like bodies to ~5–6 wt% O in CV-ox- and RC-like bodies. These predicted O contents are first-order estimates, as both the higher experimental temperature (1350 °C vs. ~988–1200 °C during percolative core formation in planetesimals) and the absence of Ni in our metallic melts would likely overestimate O solubility in natural systems.

1. Introduction

Metallic core formation appears to have been common among rocky bodies in the Solar System, but the mechanisms driving it differed between the earliest and later stages of planetary growth. During later stages, core formation likely occurred within magma oceans generated

* Corresponding authors.
E-mail addresses: varun.manilal@yale.edu (V. Manilal), damanveer.grewal@yale.edu (D.S. Grewal).

https://doi.org/10.1016/j.gca.2026.06.018
Received 24 February 2026; Accepted 12 June 2026
Available online 15 June 2026

by intense heat pulses from high-energy impacts (Tonks and Melosh, 1992). In contrast, internal heating in the earliest planetesimals was primarily driven by ^{26}Al-decay ($t_{1/2} = 0.717$ Myr; Urey, 1955; Keil et al., 1997; Hevey and Sanders, 2006), producing a thermal evolution spanning a few to ~10 Myr (Sahijpal et al., 1995, 2007; Bennett and McSween, 1996; Ghosh and McSween, 1998; Hevey and Sanders, 2006; Merk et al., 2002; Monnereau et al., 2023; Moskovitz and Gaidos, 2011; Neumann et al., 2012). While the resulting thermal evolution of individual bodies varied with both size and accretion age, metallic Fe-FeS was invariably the first major refractory phase to melt, with the onset of melting occurring at the eutectic (~988 °C at 1 bar; Bromiley, 2023; Buono and Walker, 2011). The resulting density contrast between S-rich metallic melts and the surrounding silicate matrix may have enabled downward migration of metallic melts before widespread silicate melting occurred (Ghosh and McSween, 1998; Yoshino et al., 2003; McCoy et al., 2006; Roberts et al., 2007; Terasaki et al., 2008; Ghanbarzadeh et al., 2017; Néri et al., 2019; Bromiley, 2023; Crossley et al., 2025). Textural and geochemical evidence for early segregation of S-rich metallic melts is preserved in primitive achondrites and iron meteorites (Goodrich et al., 2013; Kruijer et al., 2014; Crossley et al., 2025; Grewal et al., 2025b), indicating that core formation processes were already underway in early Solar System planetesimals before the onset of widespread silicate melting.

This early metal segregation proceeded through grain-scale percolation of metallic melts (Stevenson, 1988; Shannon and Agee, 1996; Yoshino et al., 2003; Roberts et al., 2007), which requires an interconnected metallic network within the solid silicate matrix (Bulau et al., 1979; von Bargen and Waff, 1986; Stevenson, 1988; Ghanbarzadeh et al., 2017). Whether such connectivity is achieved depends on the wetting properties of the metallic melt (Gaetani and Grove, 1999; Rose and Brenan, 2001; Terasaki et al., 2005), characterized by the dihedral angle, which is determined by the ratio of interfacial energies:

$$\theta = 2\cos^{-1}\left(\frac{\gamma_{ss}}{2\gamma_{sm}}\right) \quad (1)$$

where γ_{ss} and γ_{sm} are the solid-solid and solid-melt interfacial energies, respectively. When $\theta < 60°$, an interconnected melt network is energetically favorable at extremely low melt fractions (<1 vol%; Ghanbarzadeh et al., 2017), whereas, for $\theta > 60°$, a minimum melt fraction is required to establish interconnection. Eq. (1) assumes isotropic interfacial energies, whereas silicate minerals, particularly olivine, exhibit moderate anisotropy (Waff and Faul, 1992; Faul, 1997). Nevertheless, 2-D dihedral angle measurements in olivine aggregates have been validated as reliable proxies for 3-D melt connectivity through X-ray computed tomography studies (Roberts et al., 2007).

The interfacial energy relationships between metallic melts and silicate minerals at conditions relevant for differentiation of rocky bodies have been constrained through high-pressure, high-temperature experiments (e.g., Ballhaus and Ellis, 1996; Shannon and Agee, 1996; Bruhn et al., 2000; Yoshino et al., 2003, 2004; Terasaki et al., 2005; Walte et al., 2011; Tauber et al., 2023). Percolation of S-poor metallic melts is associated with high dihedral angles ($\theta > 90°$), requiring large melt fractions (up to ~12–25 vol%) to achieve melt connectivity (Laporte and Provost, 2000; Ghanbarzadeh et al., 2017; Néri et al., 2019). Experiments involving S-rich metallic melts under reducing conditions ($fO_2 <$ IW; IW being the Iron-Wüstite redox buffer) also yield $\theta > 60°$, indicating that such melts do not wet the silicate matrix at low melt fractions (Ballhaus and Ellis, 1996; Shannon and Agee, 1996; Holzheid et al., 2000). By contrast, anion-rich metallic melts containing both O and S under oxidizing conditions ($fO_2 >$ IW) can effectively wet the silicate matrix ($\theta < 60°$) and form an interconnected network even at extremely low melt fractions (<1 vol%; Minarik et al., 1996; Gaetani and Grove, 1999; Rose and Brenan, 2001; Terasaki et al., 2005, 2008; Miura et al., 2025).

The O content in S-rich metallic melts is controlled by the redox state of the system: at higher fO_2, the activity of O increases, driving greater dissolution of O into the metallic melt (Gaetani and Grove, 1999; Terasaki et al., 2008). This suggests that redox state is a key factor in governing the efficacy of percolative core formation in early Solar System planetesimals. Meteorite data indicate that the fO_2 of early Solar System planetesimals spanned more than 10 log units (fO_2 from IW−8 to +3; Fig. 1). Most planetesimals from both the inner and outer Solar System reservoirs were relatively reduced ($fO_2 <$ IW; Righter et al., 2016; Grewal et al., 2024), rendering O an insignificant component of their metallic melts. However, multiple meteorite groups from both reservoirs exhibit more oxidized compositions ($fO_2 >$ IW; Fig. 1). For instance, brachinites and Rumuruti chondrites from the inner Solar System record fO_2 values of IW−0.6 to +0.4 and IW+1.4 to +2.6, respectively, while several carbonaceous chondrite groups from the outer Solar System exhibit fO_2 values ranging from IW to IW+3.2 (Bercovici et al., 2022; Crossley et al., 2023). In such oxidized planetesimals, O could have been a major component in early-formed S-rich metallic melts, allowing them to wet the silicate matrix and initiate core formation through percolation in the absence of silicate melting (Terasaki et al., 2008). Therefore, understanding core formation under these oxidizing conditions is crucial not only for constraining the mechanisms of metal segregation but also for predicting the resulting core compositions of oxidized planetesimals. Geochemical models predict that oxidized carbonaceous-chondrite-like planetesimals that underwent metal-silicate differentiation would have formed S-rich metallic cores (21–35 wt% S; Bercovici et al., 2022). Yet, if percolative core formation was prevalent in these bodies, their cores could have incorporated substantial O alongside Fe and S − a feature that remains unconstrained. Such O-bearing metallic cores could profoundly influence core densities, thermal conductivity, solidification behavior, and the potential for core convection and dynamo activity (Helffrich and Kaneshima, 2004; Bromiley, 2023).

Assessing whether percolative core formation could operate in these oxidized planetesimals requires experimental constraints on the wetting properties and compositions of Fe-O-S melts at relevant conditions. Several studies have examined the percolation of metallic melts through olivine aggregates at comparable fO_2. Experiments conducted at ambient pressure show that Fe-O-S melts can effectively wet olivine with $\theta < 60°$ (Gaetani and Grove, 1999; Rose and Brenan, 2001). High-pressure experiments (P = 1.5–20 GPa; Terasaki et al., 2008, 2005) have demonstrated that O solubility in Fe-O-S melts is strongly pressure-dependent, with O content increasing as pressure decreases (Urakawa et al., 1987; Terasaki et al., 2008). The increase is most pronounced at $P < 3$ GPa, where Fe-O-S melts can contain up to ~8–10 wt% O and consistently display $\theta < 60°$ with coexisting olivine (Terasaki et al., 2008). However, both the O content of Fe-O-S melts and their corresponding dihedral angles with the silicate matrix remain poorly constrained at pressures typical of planetesimal interiors ($P < 1.5$ GPa). In particular, it remains unknown whether the O content continues to systematically increase at these lower pressures, and whether such melts maintain $\theta < 60°$ necessary for percolation. Additionally, the quantitative relationship between the fO_2 of the system, which is reflected in the FeO content of olivine, and the resulting melt composition remains unconstrained at these conditions. Without these critical constraints, we can neither assess whether oxidized planetesimals differentiated through percolation or required silicate melting, nor can we predict the compositions of their metallic cores. To address these gaps, we conducted 8 high-P-T experiments yielding 21 experimental charges to quantify O solubility in Fe-S metallic melts and to measure dihedral angles between these melts and crystalline olivine at pressures of 0.5–2 GPa and a temperature of 1350 °C. Olivine was selected as the representative silicate phase because it is the principal constituent of oxidized chondritic materials (Walker and Cameron, 2006; Dunn et al., 2010; Bischoff et al., 2011). The FeO content of olivine serves as a proxy for system fO_2, with higher FeO indicating more oxidizing conditions. Because the relationship between olivine composition and O content in

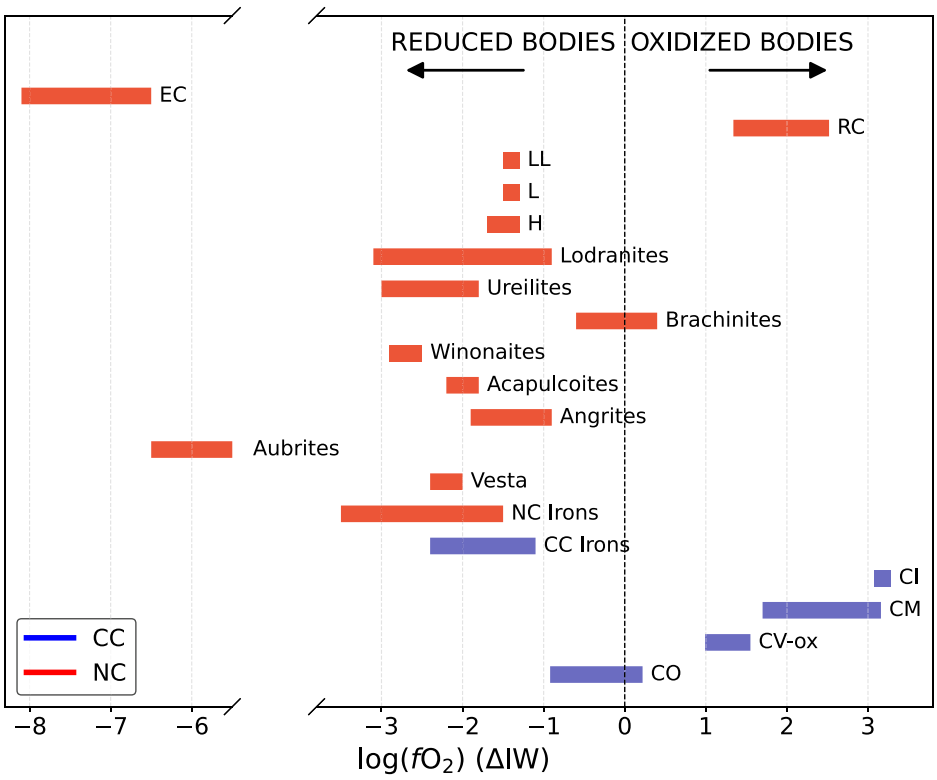

Fig. 1. Oxygen fugacity (fO_2) values of carbonaceous chondrites, ordinary chondrites, Rumuruti chondrites, enstatite chondrites, primitive achondrites, differentiated achondrites, iron meteorite parent bodies, and 4 Vesta relative to the iron-wüstite (IW) redox buffer. The fO_2 values are calculated using renormalized compositions after removing H_2O and C from the bulk compositions (see **Supplementary Text S2**). CC and NC denote carbonaceous and non-carbonaceous groups, respectively. Groups with fO_2 above the IW buffer are classified as oxidized, while those below are reduced. Early planetesimals span nearly 10 log units in redox state (fO_2 = IW–8 to +3), with most planetesimals showing reduced redox state. Bar lengths indicate 1σ about the mean value. Data and references are reported in **Supplementary Table 1**.

coexisting Fe-O-S melts at these pressures remains poorly constrained, our experiments span a broad range of olivine compositions (0–30 wt% FeO, corresponding to Fe# (mol% FeO/(FeO + MgO)) of 0–34). The 0 wt % FeO endmember (pure forsterite) serves as a baseline control for understanding the fundamental Fe-O-S-olivine equilibrium under reducing conditions, while the 15–30 wt% FeO range encompasses the silicate FeO contents characteristic of all oxidized chondrites (Jarosewich, 2006; Bischoff et al., 2011). Most experiments used Fe-FeS eutectic metal starting compositions to simulate the initial melt produced during heating of chondritic materials. An additional set of experiments employed FeS starting compositions to simulate metallic melt compositions in highly oxidized bodies, such as CM and CI chondrites, that contain little to no free metallic Fe (Jarosewich, 2006). We use these experimental results to evaluate the efficacy of percolative core formation in oxidized planetesimals accreting materials similar to carbonaceous and Rumuruti chondrite parent bodies, and to infer the compositions of their resulting metallic cores. This study constitutes Part I of a series: Part II will extend the investigation to pyroxene-bearing matrices, and Part III will examine mixed olivine-pyroxene systems representative of natural chondritic lithologies.

2. Experimental methods

Experiments were performed using starting mixtures of synthetic olivine and iron sulfide ($Fe_{1.46}S$ or stoichiometric FeS) components, prepared separately and mixed under ethanol in an agate mortar for ~40 min. Olivine was not pre-synthesized but instead formed in situ within the capsule from stoichiometric mixtures of reagent-grade (99.5–99.9%) SiO_2, MgO, and FeO powders during the high-*P*-*T* experiments. At our run conditions (1350 °C, 30 h), olivine crystallization and equilibration with the Fe-O-S melt proceed simultaneously. The resulting olivine compositions were verified by EPMA to match target values within analytical uncertainty, and their compositional homogeneity within each sample (Table 1) confirms complete reaction of the starting oxides.

To investigate the effect of FeO content in the silicate phase, we adjusted the fayalite-to-forsterite ratio to produce six compositions with FeO contents of 0, 5, 10, 15, 20, and 30 wt%. This resulted in Fe# ranging from 0 to 34. Two iron sulfide compositions were utilized: a eutectic-like $Fe_{1.46}S$ (starting composition of the eutectic experiments of Holzheid et al., 2000), and stoichiometric FeS. The $Fe_{1.46}S$ starting material was synthesized by mixing elemental reagent-grade (99.9%) Fe and FeS powders in the appropriate proportions. Following previous studies (Terasaki et al., 2005, 2008; Tsuno et al., 2024), the olivine-to-sulfide volume ratio was fixed at 98:2 to ensure that metallic melt remained below the connectivity threshold in systems with $\theta > 60°$.

Experiments were performed in a 1/2-inch end-loaded piston-cylinder apparatus at the Experimental Petrology and Igneous Processes Center (EPIC), Arizona State University (ASU). To maximize experimental efficiency, we employed a triple-capsule design in which three distinct starting compositions (varying in olivine FeO content or sulfide composition) were loaded into a single graphite capsule in separate drilled cavities (Tsuno et al., 2018; Grewal et al., 2019a, 2019b, 2021a, 2021b). Graphite capsules were selected following previous studies of metallic melt percolation in olivine aggregates (Minarik et al., 1996; Terasaki et al., 2005, 2008; Solferino and Golabek, 2018; Miura et al., 2025). Although graphite can impose reducing conditions via the C-CO buffer in some configurations (Medard et al., 2008), our experiments are internally buffered by the olivine-metal-sulfide assemblage: O contents in the Fe-O-S melt vary systematically from < 1 to > 12 wt% as a

Table 1
Summary of electron microprobe analyses (in wt%).

Exp. No.	P (GPa)	Olivine					Fe-O-S melt				
		SiO_2	MgO	FeO	Fe#[1]	No. of analyses	Fe	S	O	ΔIW	No. of analyses
Eutectic Experiments											
R150S1	1.0	40.18 (0.50)[2]	49.09 (0.29)	10.44 (0.22)	10.66	9	64.72 (1.69)	26.71 (2.00)	7.40 (1.84)	1.45[3]	11
R150S2	1.0	38.46 (0.62)	40.40 (0.52)	21.19 (0.61)	22.74	10	65.10 (0.64)	24.45 (1.83)	8.31 (1.02)	1.44	15
R150S3	1.0	42.04 (0.22)	53.38 (0.48)	5.65 (0.46)	5.60	10	61.77 (0.44)	35.87 (1.77)	0.39 (0.50)	–3.56	4
R151S1	2.0	37.88 (0.67)	38.95 (0.66)	21.40 (0.84)	23.56	9	64.42 (1.73)	24.53 (2.13)	10.41 (1.97)	2.82	13
R151S2	2.0	41.33 (0.62)	47.94 (0.41)	10.59 (0.33)	11.03	10	62.90 (0.51)	30.38 (2.95)	6.59 (1.56)	2.11	7
R151S3	2.0	41.92 (0.48)	51.85 (0.38)	6.12 (0.48)	6.21	9	61.40 (0.81)	36.64 (0.45)	0.27 (0.43)	–3.84	15
R152S1	0.75	42.23 (1.07)	53.47 (0.33)	5.12 (0.28)	5.09	9	62.82 (1.23)	29.40 (2.11)	5.14 (1.56)	0.84	12
R152S2	0.75	41.29 (0.93)	48.87 (0.46)	10.33 (0.13)	10.60	9	64.92 (1.04)	25.38 (2.18)	8.21 (1.84)	1.53	14
R152S3	0.75	39.06 (0.93)	40.72 (0.33)	20.78 (0.30)	22.25	10	65.30 (0.86)	25.51 (1.69)	7.77 (1.27)	1.32	12
R154S1	1.0	41.48 (0.62)	57.24 (0.21)	1.04 (0.06)	1.01	9	62.52 (0.65)	36.37 (0.70)	0.23 (0.42)	–4.20	8
R154S2	1.0	39.11 (0.72)	45.64 (0.30)	15.03 (0.21)	15.59	10	63.81 (1.11)	26.55 (2.23)	8.02 (1.18)	1.96	8
R155S1	0.5	39.48 (0.88)	41.46 (0.73)	19.96 (0.83)	21.26	10	65.02 (0.98)	24.27 (2.61)	9.61 (1.75)	2.2	10
R155S2	0.5	42.36 (0.87)	53.48 (0.38)	5.51 (0.31)	5.46	10	60.83 (1.36)	33.99 (1.89)	2.16 (0.94)	–0.62	5
R155S3	0.5	41.95 (0.45)	49.95 (0.15)	9.75 (0.26)	9.87	9	64.44 (1.69)	27.08 (1.45)	7.83 (1.07)	1.86	12
R156S1	1.0	37.38 (0.38)	36.02 (0.21)	26.99 (0.19)	29.60	14	63.07 (2.03)	24.83 (3.16)	12.09 (1.98)	3.88	9
FeS Experiments											
R148S1	1.0	39.58 (0.53)	41.35 (0.43)	18.66 (0.56)	20.20	10	66.37 (1.44)	32.59 (2.50)	2.72 (0.98)	–	13
R148S2	1.0	41.39 (0.64)	49.02 (0.58)	10.04 (0.54)	10.30	10	63.33 (0.85)	36.25 (0.79)	0.78 (0.37)	–	11
R148S3	1.0	41.90 (0.77)	53.05 (0.20)	4.98 (0.15)	5.01	9	64.69 (0.52)	36.94 (0.12)	0.55 (0.16)	–	15
R149S1	2.0	42.04 (0.65)	53.89 (0.27)	5.05 (0.09)	5.00	10	64.86 (0.39)	35.85 (0.93)	1.06 (0.43)	–	7
R149S2	2.0	39.45 (0.61)	42.21 (0.30)	19.03 (0.21)	20.18	10	64.50 (2.17)	32.21 (1.34)	4.42 (1.40)	–	7
R149S3	2.0	40.86 (0.60)	49.54 (0.29)	10.11 (0.12)	10.27	10	64.14 (0.75)	36.13 (0.66)	0.96 (0.63)	–	7

1. Fe# is the mol% of FeO/(FeO + MgO).
2. Numbers in brackets indicate the standard deviations.
3. The fO_2 w.r.t the IW buffer is calculated using Kress's thermodynamic model for sulfide melts (Kress, 1997, 2000, 2007). The fO_2 for FeS experiments has not been calculated because the model is only applicable to metallic Fe-rich systems. The fO_2 at the IW buffer was calculated using the fO_2 buffer calculator by Iacovino (2021).

function of olivine FeO content, and calculated fO_2 values span ~IW–4 to IW+4 (Table 1) – far wider than a restricted range expected from graphite buffering. This range reflects internal buffering by FeO exchange between olivine (~98 vol% of each charge) and the metallic melt.

The graphite capsule was enclosed in MgO, jacketed in a sintered $BaCO_3$ sleeve, and wrapped in Pb foil (**Fig. S1**). All experiments were conducted at 1350 °C and pressures of 0.5–2 GPa for 30 h. Although the Fe-FeS eutectic temperature is ~988 °C at 1 bar, the higher experimental temperature ensures attainment of textural and compositional equilibrium in the olivine-melt system, which previous studies indicate is achieved within 12 h under similar conditions (Shannon and Agee, 1996; Terasaki et al., 2005, 2008). Each assembly was cold-pressurized to the target pressure, heated at 100 °C/min to the target temperature, and quenched after 30 h by shutting off power to the furnace. For experiments below 0.75 GPa, temperature was controlled via thermocouple feedback for the initial 5 h, then switched to constant power mode for the remainder of the run to avoid temperature drift from potential thermocouple oxidation. We note that the compression-decompression procedure of Miura et al. (2025) was not adopted for low-pressure experiments owing to possible hysteresis from friction and deformation (Bose and Ganguly, 1995). Temperature was monitored using a Type D W_3Re_{97}-$W_{25}Re_{75}$ thermocouple with an accuracy of ± 10 °C (Médard and Grove, 2006).

Recovered samples were mounted in Petroepoxy, ground with sandpaper (up to 1500-grit) to expose horizontal sections, and subsequently polished with a 1 μm diamond slurry. After carbon-coating, the samples were analyzed via wavelength dispersive X-ray spectroscopy (WDS) using a JXA-8530F electron microprobe at the Eyring Materials Center, ASU. Olivine and metal-sulfide phases were analyzed in separate sessions. Metallic phases were analyzed at an accelerating voltage of 20 kV and a beam current of 15nA, whereas silicate phases were analyzed at 15 kV and 15nA. For all elements, counting times were 20 s on peak and 10 s on each background, with the exception of O (60 s and 30 s, respectively). For metallic phase analyses, Fe metal, Fe_2O_3, and FeS were used as standards for Fe, O, and S, respectively, utilizing LIFH (Fe), PETJ (S), LDE1H (O) crystals. For olivine grains, synthetic fayalite and San Carlos olivine served as standards for Fe, Si, and Mg, using TAP for (Si), TAPH (Mg), and LIF (Fe) crystals. Typical detection limits were 0.01 wt% for Si and Mg, 0.02 wt% for S and O, and 0.04 wt% for Fe.

Oxygen analysis in metallic phases presents significant analytical challenges because measurements are highly sensitive to background determination, and peak positions can vary between standards and samples (Liang, 1991; Fonseca et al., 2008). These analytical challenges are well-documented in previous experimental studies of Fe-O-S systems (Gaetani and Grove, 1999; Terasaki et al., 2005, 2008). Following the methodology of these studies, we used Fe_2O_3 as the O standard for metal analyses to minimize analytical artifacts associated with peak shifts. A beam size of 1–5 μm in diameter was used for metallic phases to account for compositional heterogeneity in quenched products. In some cases, particularly for O-poor metallic phases, the interaction volume exceeded the melt pool size, potentially affecting individual measurements. To address this limitation, up to 15 analyses were collected per sample, targeting different melt pockets across the capsule. Analyses showing evidence of olivine contamination (e.g., anomalous Si or Mg) were discarded, yielding 4–15 retained measurements per sample. The reproducibility of compositions across multiple melt pools (typically within ± 2 wt% for O; Table 1) confirms that interaction volume effects do not systematically bias the reported averages. All reported O contents in the Fe-O-S melts are blank-corrected values, obtained by subtracting the O blank determined from analyses of FeS standards (0.33 wt% O). Several experiments at low fO_2 (R150S3, R151S3, R154S1) yield blank-corrected O contents with standard deviations equal to or exceeding the mean value (Table 1), indicating that these measurements are effectively at or below the detection limit.

2-D backscattered electron (BSE) images were collected to measure dihedral angles between silicate and sulfide phases at magnifications of 1000-4000×, chosen to resolve grain-boundary triple junctions at the scale of the melt pockets, which vary from 5-50 μm (Terasaki et al., 2008; Néri et al., 2019), depending on sulfide melt pool size. Following the protocol of previous studies (Terasaki et al., 2005, 2008), dihedral angles were determined from more than 100 measurements in each sample, except R150S2 and R154S2 (75 and 86 measurements, respectively). Angles were measured using "ImageJ" software, and the median

of each dataset was taken as the representative dihedral angle. The median is preferred over the arithmetic mean because dihedral angle distributions are typically positively skewed making the median a more robust estimate of the true equilibrium angle. The measurement error was determined using a 95% confidence interval centered on the population median (Holness and Lewis, 1997). Full dihedral angle distributions and statistical parameters are provided in the **Supplementary Text (Fig. S2, Fig. S3)**.

3. Results

3.1. Textures of experimental products

All experimental products contain quenched Fe-O-S melts distributed along olivine grain boundaries and at triple junctions (Fig. 2, Fig. 3, Fig. S4). Olivine in each retrieved sample is compositionally homogenous. Multiple analyses of different metallic melt pools and olivine grains within individual experiments yielded consistent compositions within analytical uncertainty, confirming that textural and chemical equilibrium was achieved within the 30 h experimental duration. The distribution and connectivity of Fe-O-S melt vary systematically with olivine FeO content. At FeO > 5 wt%, the eutectic melt forms elongated, moderately connected networks (Fig. 2**B-C, E-F, H-I, K-L, N-O**), whereas at lower FeO, the melt remains isolated in discrete pockets (Fig. 2**A, D, G, J, M**). A similar distinction is observed in FeS experiments, where samples with FeO content greater than 10 wt% show elongated and connected Fe-O-S melt networks **(**Fig. 3**C, F)**, in contrast to those with a lower FeO content **(**Fig. 3**A-B, D-E)**. Olivine grain sizes increase systematically with FeO content, ranging from ~30 ± 10 μm at 5 wt% FeO (Fig. 2**A, D, G, J**) to ~50 ± 15 μm at 30 wt% FeO (Fig. 2**O**). This grain coarsening is consistent with enhanced grain growth driven by lower solidus temperatures characteristic of FeO-rich olivine compositions (Nichols and Mackwell, 1991; Zhao et al., 2009; Qi et al., 2021). However, grain coarsening does not influence melt connectivity, because in textural equilibrium, θ is fixed by the balance of solid–solid and solid–liquid interfacial energies and is insensitive to grain size (von Bargen and Waff, 1986). Consistent with previous studies (Gaetani and Grove, 1999; Terasaki et al., 2005, 2008), tiny blebs (~1 μm in diameter) are observed within the Fe-O-S phase at higher FeO contents (>5 wt%), interpreted as O-rich exsolution products formed during quenching (Minarik et al., 1996; Gaetani and Grove, 1999; Terasaki et al., 2005, 2008). At very high olivine FeO content (~27 wt%), FeO forms a continuous layer (~2 μm width) at the Fe-O-S melt-olivine interface and olivine-olivine grain boundaries (Fig. 2**O, Fig. S5**).

3.2. Variation of fO_2 with composition

Similar to Terasaki et al. (2008), fO_2 values for eutectic experiments were calculated using the thermodynamic model for sulfide melts developed by Kress (1997, 2000, 2007). In this model, Fe-O-S melts are treated as equilibrium solutions of six components (S, Fe, FeO, $FeO_{1.5}$, FeS, and FeOS). The calculated fO_2 values range from ~IW−4 to IW+4 (Fig. 4**;** Table 1). The oxidized end of this range encompasses differentiation conditions of all oxidized meteorites, including CV-ox, RC, CM, and CI chondrites (fO_2 = IW to IW+3.2) (Fig. 1). The more reducing experiments (fO_2 = IW−4 to IW) provide an essential baseline where O dissolution into Fe-O-S melts is negligible, enabling quantification of how increasing fO_2 progressively enhances O incorporation and melt connectivity in oxidized systems. The fO_2 is buffered by the olivine-metal-sulfide equilibrium and correlates strongly with the FeO content of coexisting olivine. The relationship between olivine FeO and fO_2 is nonlinear, showing a sharp increase in fO_2 from IW−4 to IW+2 as FeO content increases from 5 to 10 wt%, followed by a more gradual rise to IW+4 at 27 wt% FeO (Fig. 4). This sigmoidal fO_2 profile reflects the underlying O solubility behavior: the sharp increase of dissolved O in sulfide melt for olivine containing 5–10 wt% FeO (Fig. 5**A**) drives the steep rise in fO_2 through the Kress model calculations, while the gradual rise in O solubility above 10 wt% FeO produces the gradual fO_2 increase at higher compositions. The Kress model is only applicable to metallic Fe-rich systems; therefore, fO_2 values are not reported for FeS experiments where the absence of free metallic Fe limits the applicability of this thermodynamic framework (Cao, 2010). Although fO_2 cannot be explicitly calculated for the FeS experiments, the olivine FeO content remains a reliable proxy for relative redox conditions, as it controls the activity of FeO in the buffering assemblage. However, because the buffering assemblage differs between eutectic and FeS experiments, fO_2 at a given olivine FeO content is not necessarily identical, and comparisons between the two systems should be regarded as first-order approximations.

3.3. Oxygen solubility in Fe-O-S melts

Table 1 summarizes the chemical compositions of the sulfide and silicate phases. The quenched melts for experiments with eutectic and FeS starting compositions (hereafter referred to as "eutectic experiments" and "FeS experiments", respectively) plotted on an Fe-O-S ternary diagram (Fig. 6**A-B**) show nearly constant Fe concentrations (~62–65 wt%) across all experiments, while S and O concentrations display complementary behavior. This pattern is more obvious in eutectic experiments where the O content increases with rising fO_2 while the S content decreases correspondingly, reflecting the inverse relationship between these two anions in Fe-O-S melts at equilibrium (Fonseca et al., 2008; Gaetani and Grove, 1999; Kress, 1997; Terasaki et al., 2005**)**. Eutectic and FeS experiments occupy distinct regions of the compositional triangle: eutectic experiments span higher O contents (up to ~8–12 wt%) at lower S contents, whereas FeS experiments are characterized by lower O contents (<5 wt%) and higher S contents, reflecting the limited availability of metallic Fe for O bonding in FeS-rich systems.

3.3.1. Effect of silicate FeO content

Oxygen solubility in eutectic Fe-O-S melts is strongly dependent on the FeO content of coexisting olivine, which serves as a proxy for fO_2. Oxygen concentration in melts from eutectic experiments ("eutectic melts" hereafter) increases sharply from ~0–2 wt% for olivine with ~5 wt% FeO to ~6–9 wt% for olivine with 10 wt% FeO, and then changes more gradually, reaching ~8–12 wt% for olivine with ~15–30 wt% FeO (Fig. 5**A**). In contrast, melts from FeS experiments ("FeS melts") exhibit lower overall O contents and a different trend (Fig. 5**B**). Oxygen solubility increases approximately linearly but with considerable scatter, rising from ~0.5–1 wt% at ~5 wt% FeO in olivine to ~3–5 wt% at ~20 wt% FeO in olivine. These results are consistent with previous observations for FeS-based systems at both ambient pressure (Gaetani and Grove, 1999) and elevated pressures (Minarik et al., 1996; Terasaki et al., 2005).

3.3.2. Effect of pressure

In the eutectic experiments and for a given olivine FeO content, O solubility in the sulfide melt remains nearly constant within the pressure range of 0.5–2 GPa (Fig. 5**C**). For instance, in Fe-O-S eutectic melts coexisting with silicates containing ~10–20 wt% FeO, O contents consistently lie in the range of ~6–10 wt% regardless of pressure. This result agrees with the observations by Terasaki et al. (2008), who showed that O solubility in eutectic melts initially increases with decreasing pressure but reaches a plateau at P <~3 GPa. Importantly, our 0.5–2 GPa data agree well with the ambient-pressure measurements for eutectic-like melts of Gaetani and Grove (1999) at comparable fO_2, suggesting O solubility remains constant across the full 0–2 GPa range, including the unexplored range of 0–0.5 GPa. In comparison, O contents in FeS melts are systematically lower than those from the eutectic experiments at all pressures (Fig. 5**D**). For instance, at ~20 wt% olivine FeO, FeS melts contain ~3–5 wt% O, whereas eutectic melts contain

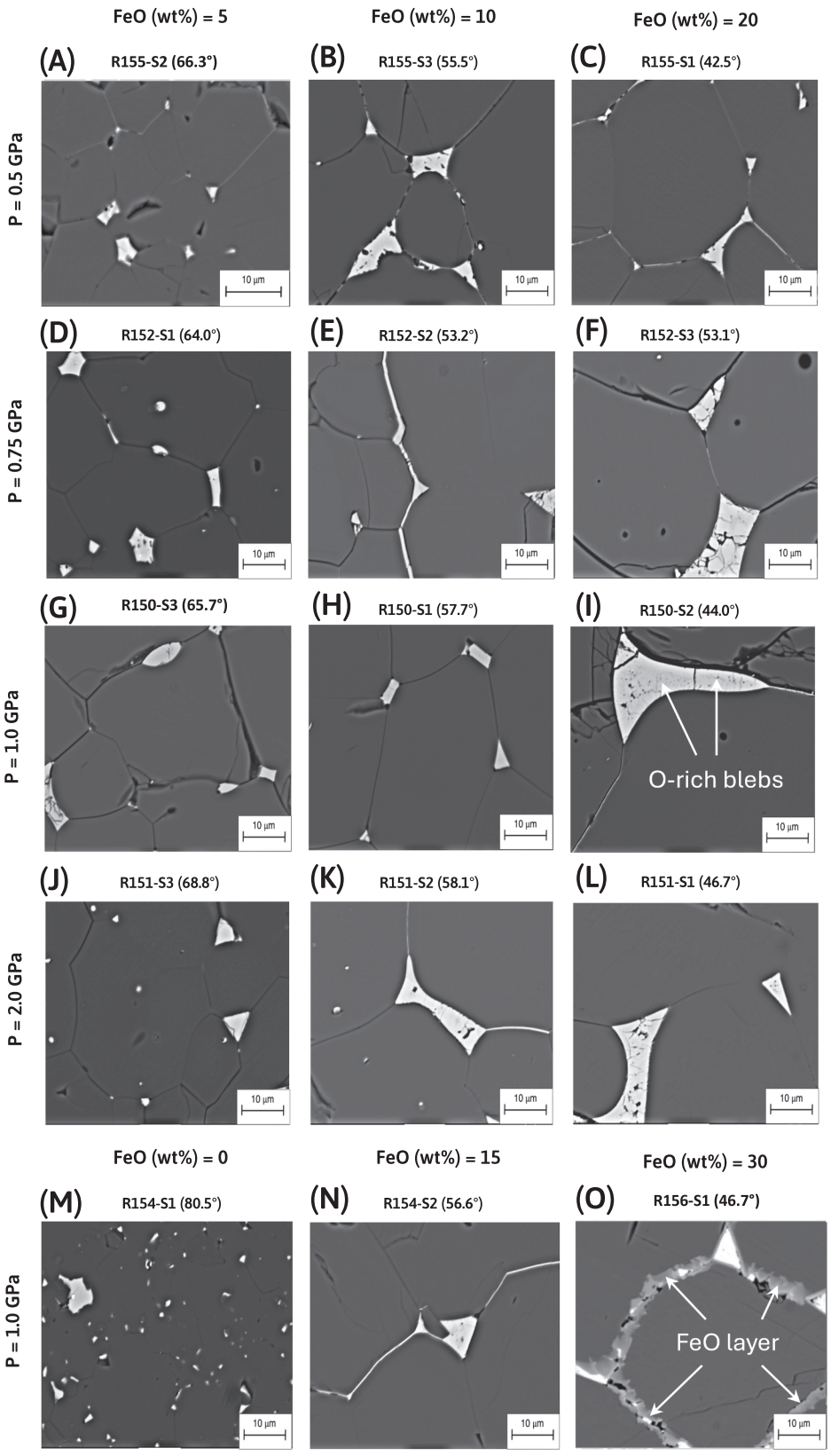

Fig. 2. Backscattered electron (BSE) images of experimental products from eutectic experiments at varying FeO contents in olivine. All samples show quenched Fe-O-S melt along olivine grain boundaries. Column headings represent initial FeO content of silicates (wt%), and rows correspond to experimental pressures. Measured dihedral angles are listed in brackets. (A-L) Experiments performed at pressures 0.5–2 GPa with 5, 10, and 30 wt% FeO. (M-O) Experiments at 1 GPa with olivine FeO contents of 0, 15, and 30 wt%. Melt structure typically transitions from isolated pockets at low FeO content (~0–5 wt%) to partially interconnected veins at higher FeO (>5 wt%). Olivine grain size increases with FeO content (30 ± 10 µm at 5 wt% FeO (A, D, G, J) to 50 ± 15 µm at 30 wt% FeO (2O)), reflecting enhanced grain growth at systematically lower solidus temperatures.

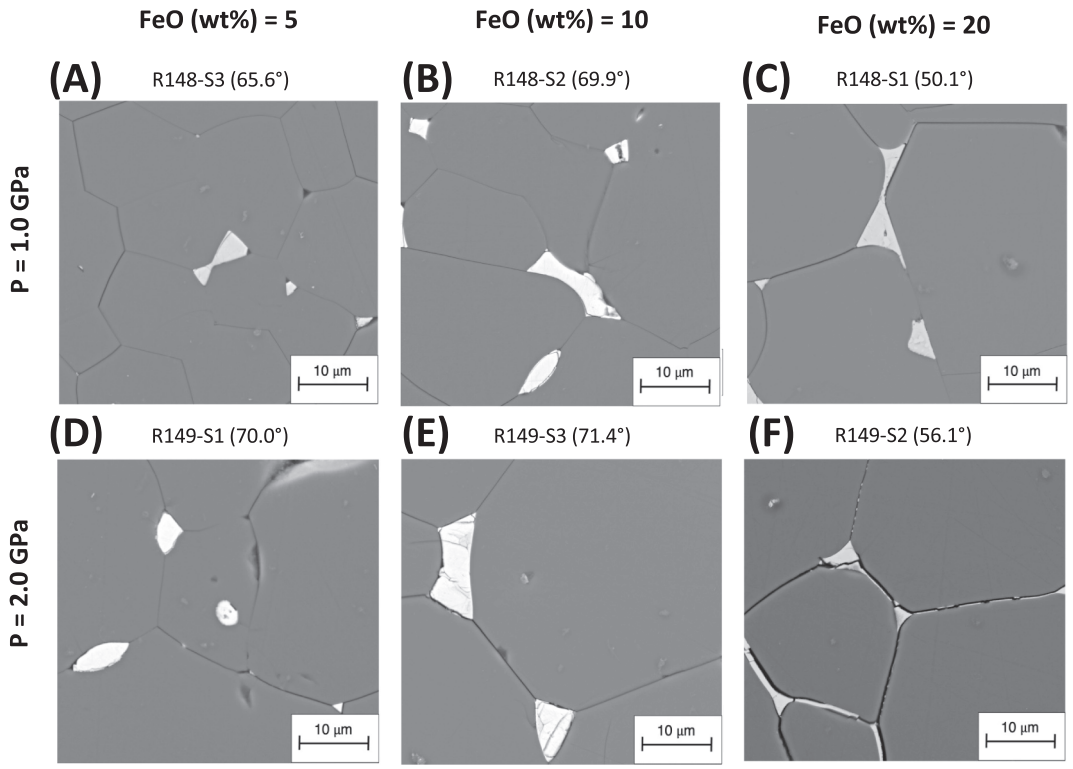

Fig. 3. Backscattered electron (BSE) images of experimental products from FeS experiments at varying FeO contents in olivine. All samples show quenched Fe-O-S melt along olivine grain boundaries. Column headings represent the initial FeO content of the silicate (wt%), and rows correspond to experimental pressures. Measured dihedral angles are listed in brackets. (A-F) Experiments were performed at pressures of 1–2 GPa with FeO content in olivine of 5, 10, and 20 wt%.

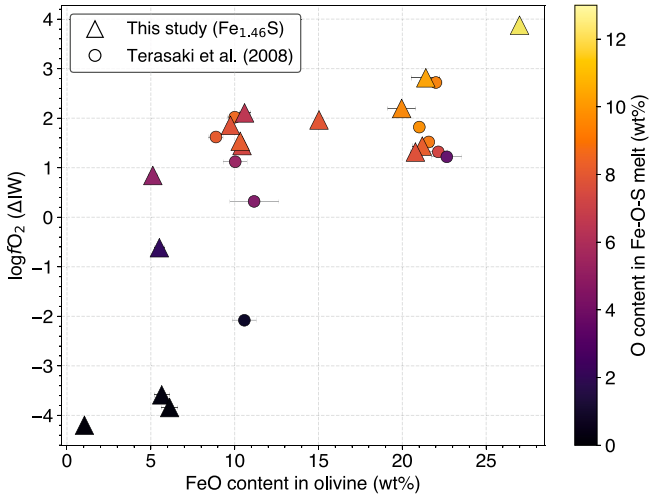

Fig. 4. Calculated log fO_2 (relative to the IW buffer) as a function of the FeO content of coexisting olivine. The color scale bar indicates O content in Fe-O-S melt. The profile exhibits a sigmoidal shape: a sharp increase in fO_2 from IW−4 to IW+2 occurs as the FeO content in olivine increases from 5 to 10 wt%, driven by enhanced O solubility, followed by a gradual rise to IW+4 at 27 wt% FeO. Values are derived using the thermodynamic model of Kress (1997, 2000, 2007) for eutectic melts. Error bars for FeO content in olivine represent 1σ deviation from the mean determined by electron microprobe analyses.

~8–10 wt% O. Previous FeS-based experimental studies also reported similar O contents (Minarik et al., 1996; Gaetani and Grove, 1999; Terasaki et al., 2005). Within the 0.5–2 GPa pressure range, O contents in Fe-O-S melts of FeS experiments show no systematic variation with pressure. This observation is consistent with previous data across pressures from 1 atm to 4.6 GPa (Minarik et al., 1996; Gaetani and Grove, 1999; Terasaki et al., 2005).

3.4. Parameters controlling the dihedral angle

Dihedral angles (θ) as a function of FeO content and total anion/total cation ratio are summarized in Table 2.

3.4.1. Dependence on FeO content in olivine

In eutectic experiments, θ decreases monotonically with increasing olivine FeO content from ~80° at ~1 wt% FeO to ~46° at ~30 wt% FeO (Fig. 7**A**). Under highly reducing conditions (fO_2 < IW–2), θ is extremely high (~80°). As fO_2 increases, θ decreases progressively, with a more gradual decline in the range fO_2 = IW−2 to IW+1 (Fig. 8). The critical interconnection threshold (θ < 60°) is reached at ~10 wt% FeO, corresponding to fO_2 > IW+1. The decline in θ is steepest between 5 and 10 wt% FeO, coinciding with the rapid increase of O content in the eutectic melt (Fig. 7**A**). Notably, θ continues to decline from ~50-60° at 10 wt% FeO to ~40-50° at 20–27 wt% FeO (Fig. 7**A**) even though the O content in the eutectic melt does not increase as sharply as the O content in samples containing ~5–10 wt% FeO olivine (Fig. 5**A**). We note that the data from Terasaki et al. (2008) at P > 3 GPa plot systematically above the trend defined by our eutectic experiments (Fig. 7**A**), consistent with reduced O solubility and higher θ values at elevated pressures.

Overall, FeS experiments display a similar trend, with θ decreasing from ~65-71° with ~5 wt% FeO olivine to ~50-56° with ~19 wt% FeO olivine; Fig. 7**B**); although θ values change little for olivine containing ~5–10 wt% FeO. The interconnection threshold (θ < 60°) is reached at a higher FeO content in olivine (~15–19 wt%) than eutectic melts (~10 wt% FeO olivine) due to systematically lower O contents in FeS melts. Data on experiments with FeS from Minarik et al. (1996) and Terasaki et al. (2005) plot at higher θ (>70°), consistent with a pressure effect on O solubility as these experiments were conducted at 3.5–4.6 GPa. The dependence of θ on O content in Fe-O-S melts (**Fig. S7**) parallels its relationship with olivine FeO content (Fig. 7**A-B**), as expected from the

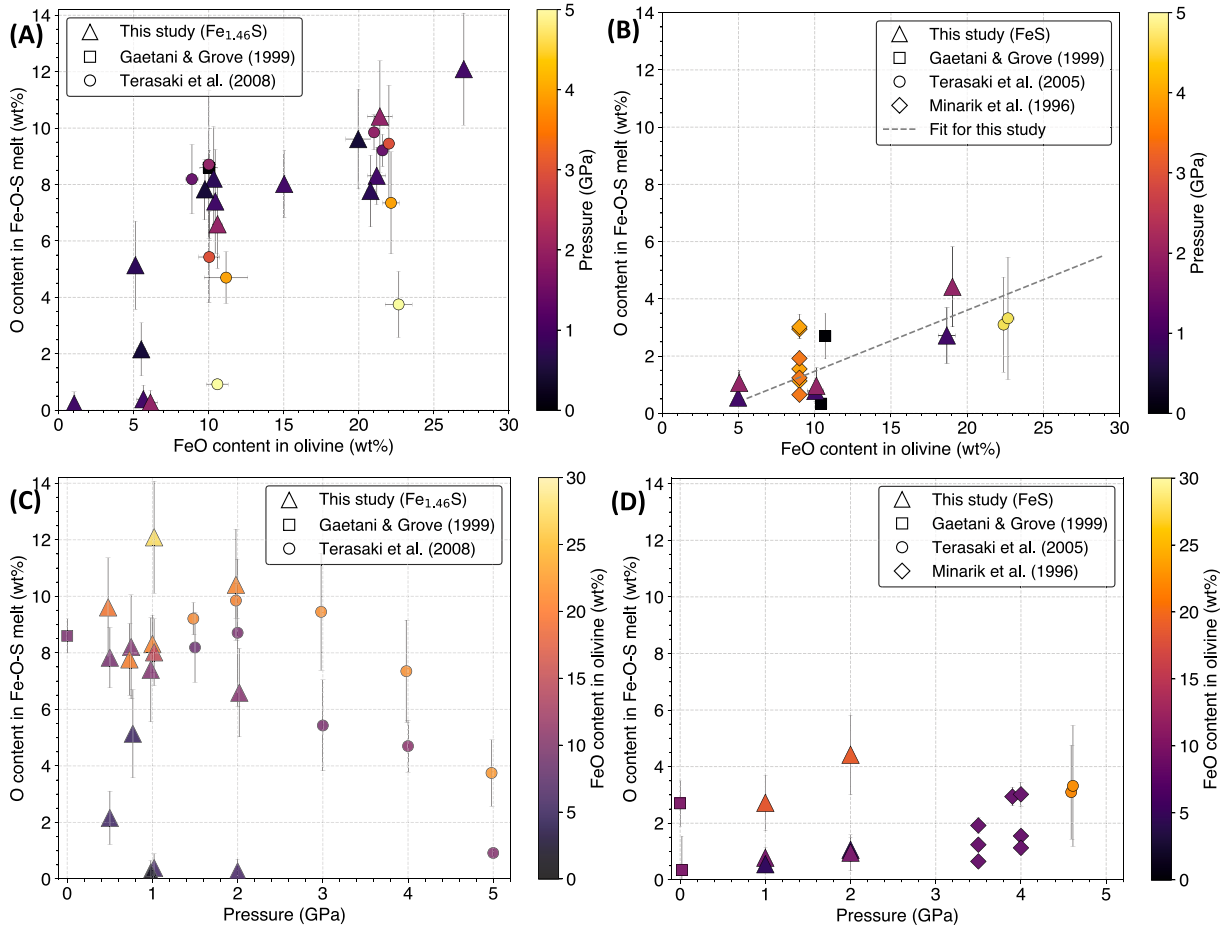

Fig. 5. Variation of O content in the Fe-O-S melt with FeO content in olivine for eutectic and FeS experiments (A-B). The color scale bar indicates pressure. (A) Oxygen content in eutectic melts vs. olivine FeO content, showing a sharp rise from ~0–2 wt% to ~6–9 wt% O between 5 and 10 wt% FeO, followed by a gradual rise. (B) Oxygen content in FeS melts vs. olivine FeO, showing a linear but lower solubility trend (<5 wt% O). Line in panel (B) depicts the best linear fit for O solubility in FeS melts for our experimental data. (C-D) Oxygen solubility plotted against pressure (0.5–2 GPa). Eutectic melts (C) maintain constant O solubility across the investigated pressure range for a given FeO content, and this solubility is similar to observations at ambient pressure (Gaetani and Grove, 1999). FeS melts (D) similarly show no systematic pressure dependence in this range. Error bars for O content in the Fe-O-S melt and FeO content in olivine represent 1σ deviation from the mean determined by electron microprobe analyses.

correlation between these parameters (Fig. 5**A-B**).

3.4.2. *Dependence on pressure*

At a given olivine composition, θ remains roughly constant or increases only slightly from 0.5 to 2 GPa for eutectic experiments (Fig. 7**C**). For olivine FeO contents of ~5, ~10, and ~20 wt%, mean dihedral angles cluster around ~66°, ~56°, and ~45°, respectively, showing minimal variation below 2 GPa. At higher pressures (>3 GPa, Terasaki et al., 2008), θ increases more steeply with pressure, displaying nearly linear positive correlations. This pressure dependence at $P > 3$ GPa reflects the systematic decrease in O solubility observed at elevated pressures (Urakawa et al., 1987; Terasaki et al., 2008). FeS experiments display two distinct clusters across P: θ ~52° for olivine FeO > 10 wt% and θ ~66° for FeO < 10 wt% (Fig. 7**B**). While Minarik et al. (1996) did not observe a clear pressure dependence, likely due to their limited pressure range (3.5–4 GPa), our dataset, combined with that of Terasaki et al. (2005), shows a positive correlation between θ and pressure across the broader 1–5 GPa range (Fig. 7**D**).

3.4.3. *Dependence on total anion/total cation ratio*

The variations in θ with composition can be characterized by considering the total anion content in the Fe-O-S melt. For eutectic compositions (**Fig. S6**), θ decreases systematically with increasing (S + O)/Fe ratio, dropping from ~100° at (S + O)/Fe ratio of ~0.6 to below ~60° at ratios above ~1.1. The data from this study overlap with the 1 bar results from Gaetani and Grove (1999) and Rose and Brenan (2001), and extends the relationship to higher anion/cation ratios. Data from Terasaki et al. (2008) at higher pressures (1.5–5 GPa) show greater scatter, reflecting the significant effect of pressure on both O solubility and θ. We note that Holzheid et al. (2000) did not measure O content in their sulfide melts, which may lead to underestimation of the true (S + O)/Fe ratios in their dataset. FeS experiments display a similar negative correlation between θ and (S + O)/Fe ratio (**Fig. S6**), with θ decreasing from ~100° at a (S + O)/Fe ratio of ~0.6 to ~55° at a ratio of ~1.1. The data from this study overlap closely with those of Terasaki et al. (2005), whereas Minarik et al. (1996) and Ballhaus and Ellis (1996) reported generally lower (S + O)/Fe ratios (<1.0) and correspondingly higher θ values (>75°). Overall, consistent with observations from previous studies (Minarik et al., 1996; Gaetani and Grove, 1999), both eutectic and FeS experiment datasets demonstrate that θ decreases consistently with increasing the anion/cation ratio across the full compositional and pressure range investigated in this study.

4. Discussion

Our experiments demonstrate that the efficacy of percolative core formation in oxidized planetesimals is primarily controlled by redox conditions (fO_2). Three key findings emerge: (1) dihedral angles fall

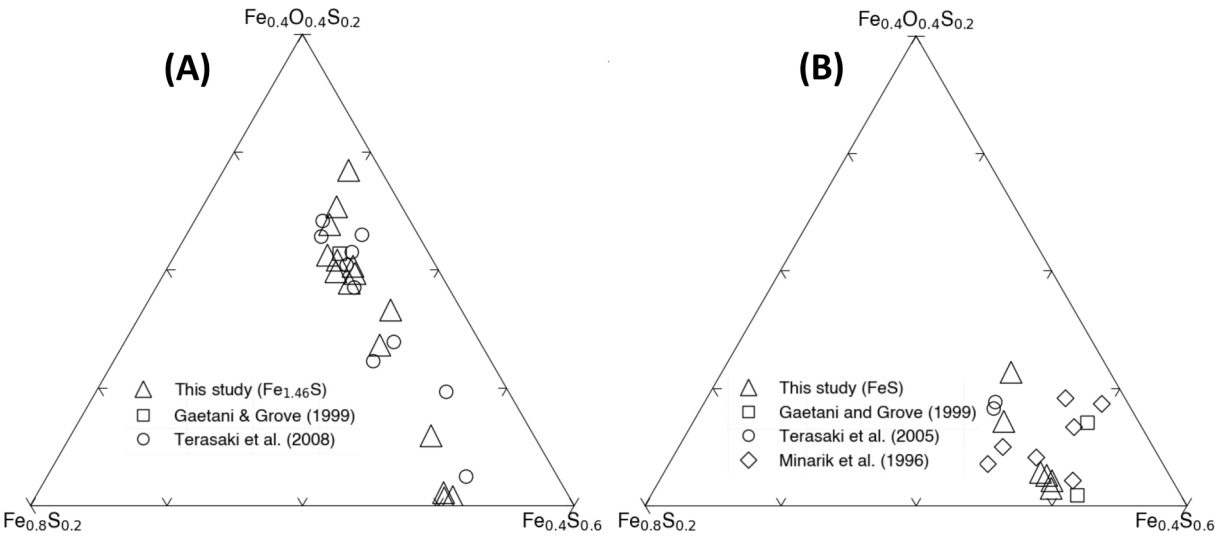

Fig. 6. Fe-O-S ternary diagram illustrating the melt compositions for (A) eutectic and (B) FeS melts analyzed in this study and compared with measurements from previous studies. O, S, and Fe contents are normalized to 100 mol.% and projected onto the ternary compositional space. (A) Filled triangles represent $Fe_{1.46}S$ experiments (this study), open circles represent compositions from Terasaki et al. (2008), and the open squares represent compositions from Gaetani and Grove (1999). (B) In experiments starting with FeS metallic composition, filled triangles represent this study. The previous studies considered are Terasaki et al. (2005) (open circles), Gaetani and Grove (1999) (open squares), and Minarik et al. (1996) (open diamonds). The diagram highlights the range of Fe-O-S melts compositions examined at 1–2 GPa. The Fe-O-S ternary diagram shows nearly constant Fe concentrations across all experiments (~62–65 wt%), while S and O concentrations show complementary behavior. Data from eutectic and FeS experiments occupy distinct regions of the compositional triangle, reflecting variations in S and O dissolution with the starting metal composition. Eutectic melts form a trend of increasing O (up to ~12 wt%) and decreasing S consistent with equilibrium exchange, whereas FeS melts cluster at lower O (<5 wt%) and higher S contents due to limited metallic Fe availability.

Table 2
Results of dihedral angle measurements and anion/cation ratios for all experimental products.

Exp. No.	Pressure (GPa)	Average FeO content in olivine (wt%)	(S + O)/Fe	No. of angles measured	Dihedral angle (degrees)	C.I. (–)[1]	C.I. (+)
Eutectic Experiments							
R150S1	1.0	10.44 (0.22)	1.12	145	57.67	54.89	59.57
R150S2	1.0	21.19 (0.61)	1.10	75	43.96	42.77	51.18
R150S3	1.0	5.65 (0.46)	1.03	149	65.70	62.59	67.53
R151S1	2.0	21.40 (0.84)	1.23	131	46.70	44.08	50.04
R151S2	2.0	10.59 (0.33)	1.21	139	58.08	54.39	59.54
R151S3	2.0	6.12 (0.48)	1.06	148	68.79	65.15	70.39
R152S1	0.75	5.12 (0.28)	1.10	142	64.01	61.45	66.58
R152S2	0.75	10.33 (0.13)	1.12	112	53.18	49.66	55.40
R152S3	0.75	20.78 (0.30)	1.10	110	53.09	49.71	54.13
R154S1	1.0	1.04 (0.06)	1.03	141	80.50	76.74	82.61
R154S2	1.0	15.03 (0.21)	1.16	86	56.64	51.93	60.42
R155S1	0.5	19.96 (0.83)	1.17	135	42.53	41.31	47.56
R155S2	0.5	5.51 (0.31)	1.10	171	66.31	63.10	67.77
R155S3	0.5	9.75 (0.26)	1.16	150	55.46	52.96	58.10
R156S1	1.0	26.99 (0.19)	1.36	120	46.67	46.15	54.26
FeS Experiments							
R148S1	1.0	18.66 (0.56)	1.00	118	50.06	48.15	55.38
R148S2	1.0	10.04 (0.54)	1.04	115	69.91	65.43	71.74
R148S3	1.0	4.98 (0.15)	1.02	116	65.57	64.27	70.02
R149S1	2.0	5.05 (0.09)	1.02	122	70.04	67.53	73.86
R149S2	2.0	19.03 (0.21)	1.11	106	56.05	52.78	58.44
R149S3	2.0	10.11 (0.12)	1.03	126	71.38	66.00	71.49

1. Error estimate on the dihedral angle was based on a 95% confidence interval (C.I.) centered on the population median (Holness and Lewis, 1997).

below the critical 60° percolation threshold once the FeO content in olivine exceeds ~10 wt% in eutectic melts (Fig. 7**A**) (corresponding to $fO_2 \gtrsim$ IW+1; Fig. 8) and ~15–19 wt% in FeS melts (Fig. 7**B**), enabling interconnected metallic melt networks to form even at low melt fractions (<1 vol%) in solid silicate matrix; (2) S and O act synergistically as surface-active elements, such that the total anion content controls interfacial energies (**Fig. S6**); and (3) pressure only has a minor effect on melt connectivity below 2 GPa, implying that redox state and metallic melt composition, rather than planetesimal size, determined whether early core formation proceeded via percolation. Below we discuss the mechanisms underlying these behaviors and their implications for core formation in oxidized planetesimals.

4.1. Mechanisms controlling O solubility in Fe-O-S melts and their connectivity

4.1.1. Thermodynamic control on O solubility in Fe-O-S melts

The strong correlation between olivine FeO content and O solubility in eutectic melts (Fig. 5**A**) reflects thermodynamic equilibrium between coexisting phases. During equilibration, the FeO component of olivine reacts with the metallic melt at the interface, driving O dissolution into the Fe-O-S liquid. Because olivine vastly dominates the phase

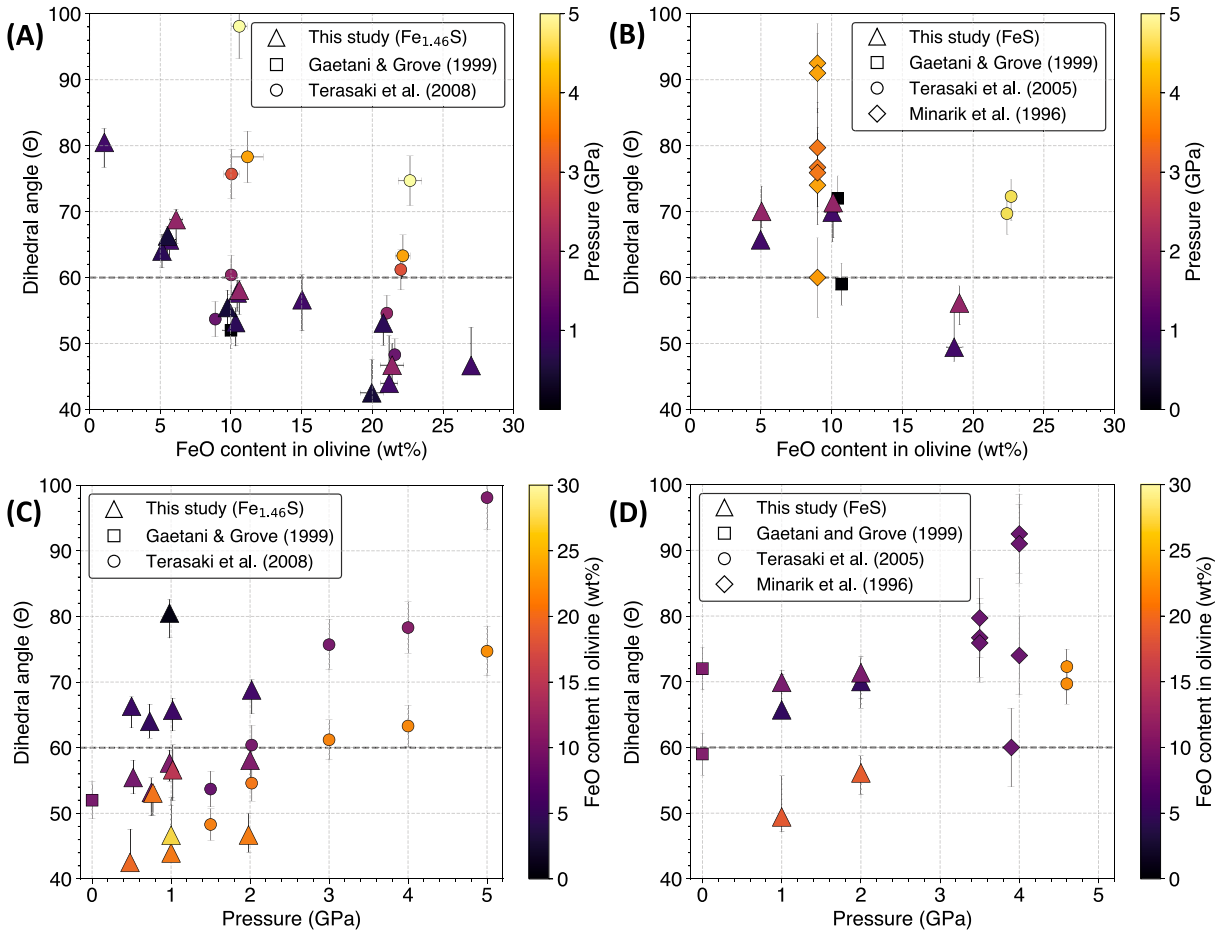

Fig. 7. Dihedral angles in Fe-O-S melts from eutectic (left) and FeS (right) experiments as a function of FeO content (A, B), with pressure in the third axis. θ decreases with increasing FeO. θ decreases sharply up to ~10 wt% FeO in eutectic melts, coinciding with rising O content in the melt, and falls more gradually at higher FeO contents. In eutectic melts, θ drops below the interconnection threshold of 60° at ~10 wt% olivine FeO (A). FeS melts show a similar wetting behavior but reach the percolation threshold at higher FeO contents (~15–19 wt%). (C-D) Variation in θ as a function of P for (C) Eutectic and (D) FeS experiments. θ remains roughly constant up to 2 GPa and increases linearly at higher P. Error bars for compositions represent 1σ standard deviation determined by electron microprobe analyses, whereas the error bars for dihedral angles are based on a 95% confidence interval centered on the population median (Holness and Lewis, 1997).

assemblage (~98 vol%), its measured composition remains within analytical uncertainty of the starting material. At equilibrium, increasing FeO content in olivine raises the activity of FeO in the silicate and, therefore, the equilibrium fO_2 buffered by the olivine-metallic melt assemblage. The higher fO_2 drives greater O dissolution into the Fe-O-S melt (Terasaki et al., 2005, 2008; Fonseca et al., 2008; Kiseeva and Wood, 2013, 2015). This thermodynamic coupling between olivine FeO, fO_2, and [O] in the melt is expressed by the two-regime relationship between log $[O]_{melt}$ vs. log fO_2 for eutectic melts (Fig. 9):

1) Low-to-intermediate oxidation states (IW–4 < fO_2 < IW+2): In this range, O solubility increases approximately linearly with log fO_2, from ~0.2 wt% at fO_2 = IW–4 to ~8–10 wt% at fO_2 = IW+2. The best-fit slope of log $[O]_{melt}$ vs. log fO_2 is ~0.3–0.4, i.e., 1-log-unit increase in fO_2 increases dissolved O by a factor of ~2–2.5. In this regime, the melt remains oxide-undersaturated: the system accommodates increasing fO_2 entirely through higher dissolved O in a single Fe-O-S melt phase, without requiring a separate oxide. This linear trend reflects the strong fO_2 dependence of O dissolution in oxide-undersaturated Fe-O-S melts.
2) Highly oxidizing conditions (fO_2 > IW+2): At higher fO_2 conditions, O solubility continues to rise but more gradually, approaching ~12 wt% at fO_2 ~IW+4. The change in slope near fO_2 ~IW+2 marks the onset of oxide saturation. At this point, the Fe-O-S melt approaches its structural solubility limit for O at the experimental temperature and bulk composition. Further increases in fO_2 cannot be accommodated solely by increasing the dissolved O content of a single melt phase. Instead, equilibrium is maintained by changing the phase assemblage: a separate FeO-rich oxide becomes stable and precipitates at melt-silicate interfaces and along grain boundaries (Fig. 2**O**, **Fig. S5**; Eustathopoulos et al., 1999). Beyond this point, the melt remains close to its saturation [O], and additional O is taken up primarily by the FeO-rich oxide phase, causing the log $[O]_{melt}$ vs. log fO_2 curve to flatten.

This behavior demonstrates that O incorporation into eutectic Fe-O-S melts is most sensitive to fO_2 changes in the IW to IW+2 range, which encompasses some of the oxidized chondrite groups (Fig. 1). The steep rise in O solubility between ~IW and IW+2 confirms the trend observed by Terasaki et al. (2008) and is consistent with ambient-pressure O dissolution in eutectic-like melts (Kress, 1997; Gaetani and Grove, 1999; Rose and Brenan, 2001). Although we cannot directly calculate fO_2 for melts from FeS experiments using the Kress model (see **Section 3.2** above), the log fO_2 vs. FeO content relation established for eutectic melts (Fig. 4) provides a first-order guide to the redox conditions expected for FeS-rich runs at the same olivine FeO content. In contrast to eutectic melts, FeS melts show a more gradual, approximately linear increase in O solubility, i.e., from ~0.5–1 wt% to ~3–5 wt%, as the FeO content in coexisting olivine increases from ~5 to 20 wt% (Fig. 5**B**). However, in the absence of metallic Fe, the buffering assemblage differs, so

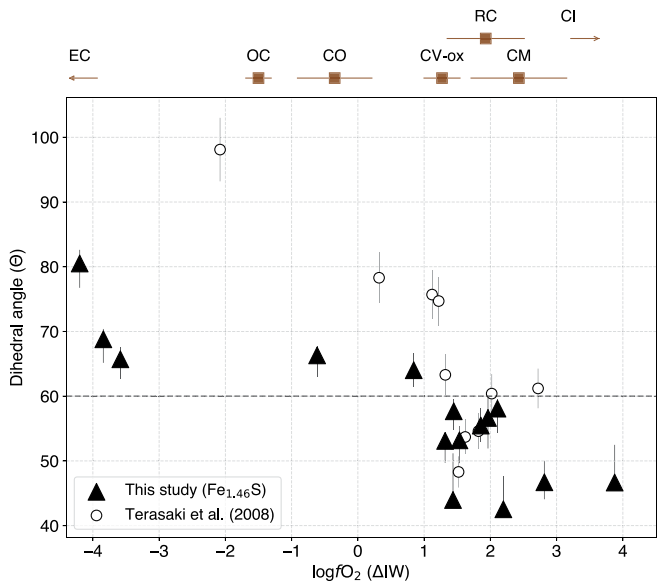

Fig. 8. Dihedral angles plotted against calculated log fO_2 for samples from eutectic experiments. The percolation threshold ($\theta < 60°$) for eutectic melts is crossed at approximately IW+1. High wetting angles (~80°) persist at reducing conditions (fO_2 < IW–3), while highly oxidized conditions (>IW+2) result in low angles (~45°). FeS experiments are excluded due to the absence of metallic Fe (see text for details). Oxygen fugacity ranges of chondrite groups plotted along the same ΔIW scale for reference. Symbols and horizontal error bars denote mean values and uncertainties for each group; vertical offsets are applied for clarity. Right-pointing arrows indicate lower-bound estimates (CI), and the left-pointing arrow marks values extending beyond the plotted range (EC).

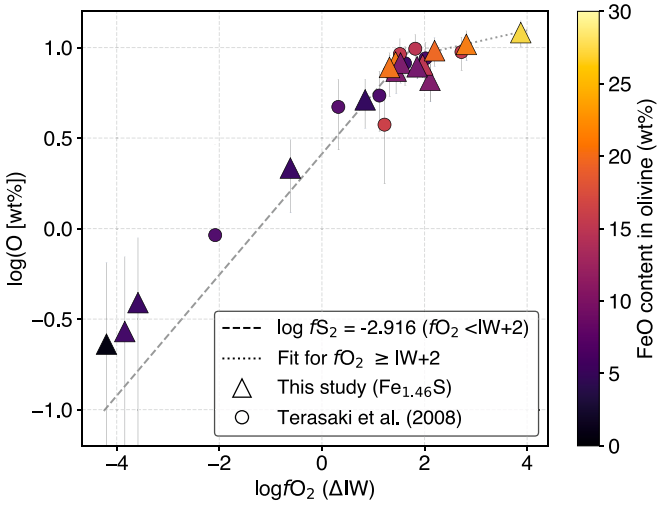

Fig. 9. Oxygen solubility in eutectic Fe-O-S melts as a function of oxygen fugacity. Symbol color indicates FeO content of the coexisting silicate (wt%). The dashed line represents the parameterization of oxygen solubility in eutectic Fe-O-S melts vs. log fO_2 fitted using the model of Fonseca et al. (2008) for fO_2 < IW+2 (see Section 4.2). The dotted line depicts the best linear fit for O solubility as a function of log fO_2 for fO_2 > IW+2.

comparisons between eutectic and FeS-rich compositions at a given olivine FeO should only be regarded as first-order approximations.

4.1.2. Langmuir model for competitive adsorption at the olivine–metal interface

The difference between eutectic and FeS melts in both the absolute level of O solubility and its dependence on FeO content in olivine (**Fig. S8**) requires a thermodynamic explanation. Terasaki et al. (2005) proposed that S and O adopt different structural roles on either side of the Fe-S eutectic. On the Fe-rich side, both S and O were proposed to act as surface-active elements (elements that lower interfacial energy). Conversely, on the FeS-rich side, S was proposed to be strongly bonded to Fe in the bulk metallic melt, reducing its surface activity, and, therefore, its ability to lower dihedral angles. Our data contradict this interpretation: when plotted against O content in the melt (**Fig. S7A, B**), FeS melts reach $\theta < 60°$ at lower O contents (~3 wt%) than eutectic melts (~6 wt%). If S were not surface-active in FeS melts, the absence of its contribution to lowering interfacial energy would require more O to achieve $\theta < 60°$, not less. The lower O threshold in FeS melts therefore indicates that the abundant S in these melts remains surface-active and contributes to wetting. An alternative framework is therefore needed to explain how both S and O contribute to wetting across the full compositional range.

To reconcile the above observations, we invoke the Langmuir model of competitive adsorption (Langmuir, 1918; Biswas et al., 2022). In this predictive framework, S and O are both surface-active elements that compete for the same interfacial binding sites at the olivine-metallic melt interface. The partitioning of S vs. O between the interface and the bulk depends on their relative activities: when the activity of S (or fS_2) ≫ O activity (or fO_2), S preferentially occupies interface sites; conversely, as O activity increases, O displaces S from these sites (Cao, 2010). At the olivine-metallic melt interface, molecular FeO transported from the bulk olivine to the interface dissociates, allowing O adsorption via:

$$[FeO]_i + \square \rightleftharpoons [Fe]_i + O_{ads} \tag{2}$$

where $[FeO]_i$ is the FeO concentration at the interface, $\square$ denotes a vacant reaction site, $[Fe]_i$ is Fe at the interface, and O_{ads} is the adsorbed O. Analogously, the adsorption of S at the interface proceeds via:

$$[FeS]_b + \square \rightleftharpoons [Fe]_i + S_{ads} \tag{3}$$

where $[FeS]_b$ is the FeS concentration in the bulk metallic melt and S_{ads} is the adsorbed S. The concentration of dissolved O in the bulk melt is controlled by the equilibrium partitioning of O between the interface and bulk and is governed by the relative coverage of O at the interface, C_O, the fraction of reaction sites occupied at the interface occupied by O (Lasaga, 2014). To first order,

$$[O]_{melt} \propto C_O \tag{4}$$

Solving for the equilibrium coverages of O and S (C_O and C_S) we obtain (for detailed mathematical treatment, see the **Supplementary Text S1**):

$$C_O = \frac{K_O^{eq} a_{FeO}^i}{a_{Fe}^i + K_O^{eq} a_{FeO}^i + K_S^{eq} a_{FeS}^b} \tag{5}$$

$$C_S = \frac{K_S^{eq} a_{FeS}^b}{a_{Fe}^i + K_O^{eq} a_{FeO}^i + K_S^{eq} a_{FeS}^b} \tag{6}$$

where C_O and C_S are the fractions of reaction sites occupied by the adsorbed O and S, respectively,

K_O^{eq} and K_S^{eq} are the equilibrium constants for O adsorption and S adsorption reactions (Eqs. (2) and (3)); a_{FeO}^i is the activity of FeO at the interface; a_{FeS}^b is the activity of FeS in the bulk melt; and a_{Fe}^i is the activity of Fe at the interface.

Eqs. (4) and (5) lead us to the key result that $[O]_{melt}$ is proportional to the activity of FeO:

$$[O]_{melt} \propto \frac{K_O^{eq} a_{FeO}^i}{a_{Fe}^i + K_O^{eq} a_{FeO}^i + K_S^{eq} a_{FeS}^b} \tag{7}$$

In FeS melts, a_{FeS}^b is higher, so the term $K_S^{eq} a_{FeS}^b$ dominates. This result

leads to greater interfacial coverage by S, limited O coverage, and therefore lower bulk O solubility that increases only modestly with FeO (and fO_2). In near-eutectic, Fe-rich melts, a^b_{FeS} is relatively low. As a result, increases in a^i_{FeO} (and thus in fO_2) have a much stronger effect on C_O and hence on $[O]_{melt}$, producing the steep log $[O]_{melt}$ vs. log fO_2 trend established for eutectic melts (Fig. 9). The observed anticorrelation between dissolved S and O contents (Fig. 6) directly reflects this competitive adsorption: as fO_2 increases at fixed fS_2, O coverage at the interface grows at the expense of S, and vice versa (**Fig. S9**). Experimental results from Gaetani and Grove (1999) support this interpretation: at similar fO_2, they obtain eutectic-like O solubilities when fS_2 is low (log $fS_2 \sim -2.5$), but FeS-like O solubilities when fS_2 is higher (log $fS_2 \sim -1.5$). This correlation is consistent with the framework that a given fO_2 can yield different bulk O contents as a function of fS_2, due to S-O competition for interfacial sites. Thus, the Langmuir competitive-adsorption framework shows that O solubility in Fe-O-S melts depends fundamentally on both fO_2 and fS_2, not on fO_2 alone, and naturally explains the different log $[O]_{melt}$ vs. log fO_2 trends and O solubility levels observed for eutectic and FeS melts (Fig. 9).

4.1.3. Dihedral angles and the transition to melt connectivity

The pattern of O incorporation into Fe-O-S melts directly controls θ and, thus, melt connectivity. To understand this relationship, we employ the Gibbs adsorption isotherm, which relates changes in interfacial composition to changes in interfacial energy (Gaetani and Grove, 1999). In differential form, the Gibbs adsorption equation at constant P, T is

$$-d\gamma_{solid-melt} = \Sigma_i \Gamma_i d\mu_i \tag{8}$$

where γ is the solid-melt interfacial energy, Γ_i is the surface excess concentration of component i, and μ_i is its chemical potential. The surface excess Γ_i represents the excess amount of component i per unit area at the interface relative to what would be present if the bulk composition extended uniformly to the surface. Written explicitly for the components in the Fe-O-S melts relevant to our experiments, Eq. (8) becomes

$$-d\gamma_{solid-melt} = \Gamma_{Fe} d\mu_{Fe} + \Gamma_O d\mu_O + \Gamma_S d\mu_S \tag{9}$$

For surface-active elements such as O and S, increasing μ_O or μ_S (via higher fO_2 and fS_2), increases their interfacial excess and, through the Gibbs adsorption equation, lowers γ and hence, θ. Oxygen has a stronger effect on lowering γ than S does because of the stronger bonding interaction of O with Fe at the interface (i.e., $\left|\frac{d\gamma}{d\mu_O}\right| > \left|\frac{d\gamma}{d\mu_S}\right|$; Cao, 2010). Consequently, as O displaces S (due to competitive adsorption), the net effect is a decrease in γ.

To focus on the dominant contributions from O and S, we combine terms using the Gibbs-Duhem relation ($\Sigma_i X_i d\mu_i = 0$) at constant T and P, and eliminate the Fe term, yielding:

$$-d\gamma = \Gamma_O^{(Fe)} d\mu_O + \Gamma_S^{(Fe)} d\mu_S \tag{10}$$

where $\Gamma_i^{(Fe)} = \Gamma_i - \left(\frac{X_i}{X_{Fe}}\right)\Gamma_{Fe}$ is the surface excess of species i relative to Fe metal at fixed T and P. In our closed systems, with no external O_2 and S_2 reservoirs, fO_2 and fS_2 are internally buffered by the activities of FeO and FeS through the redox equilibria:

$$FeO \rightleftharpoons Fe + \tfrac{1}{2}\, O_2 \tag{11}$$

$$FeS \rightleftharpoons Fe + \tfrac{1}{2}\, S_2 \tag{12}$$

The equilibrium constants for these reactions relate the activities of Fe, FeO, and FeS to the corresponding fugacities of O_2 and S_2. Rearranging the equilibrium expressions gives:

$$fO_2 = \left(\frac{a_{FeO} \cdot K_O}{a_{Fe}}\right)^2 \tag{13}$$

$$fS_2 = \left(\frac{a_{FeS} \cdot K_S}{a_{Fe}}\right)^2 \tag{14}$$

so that at equilibrium the O and S fugacities are fully determined by the activities of Fe, FeO, and FeS together with the T and P dependent equilibrium constants.

The chemical potentials of O and S can then be written explicitly in terms of their fugacities as:

$$\mu_O = \mu_O^\circ + \frac{1}{2} RT ln(fO_2) \tag{15}$$

$$\mu_S = \mu_S^\circ + \frac{1}{2} RT ln(fS_2) \tag{16}$$

where μ_i° is the standard chemical potential, R is the gas constant and T is the temperature. Differentiating these equations and substituting into Eq. (10) leads to a direct relation between changes in γ and changes in fO_2 and fS_2 (See **Supplementary Text S1** for the full derivation):

$$\frac{\partial \gamma}{\partial \ln(fO_2)}\Big|_{fS_2} = -\frac{RT}{2}\Gamma_O^{(Fe)} \tag{17}$$

$$\frac{\partial \gamma}{\partial \ln(fS_2)}\Big|_{fO_2} = -\frac{RT}{2}\Gamma_S^{(Fe)} \tag{18}$$

These expressions show that the sign and magnitude of $\Gamma_O^{(Fe)}$ and $\Gamma_S^{(Fe)}$ control how γ (and thus, θ) responds to changes in fO_2 and fS_2. When $\Gamma_S^{(Fe)} > 0$ (i.e., the interface is enriched in S relative to Fe), increasing fS_2 lowers γ and θ, whereas when $\Gamma_S^{(Fe)} < 0$ (i.e., the interface is depleted in S), increasing fS_2 raises γ and θ. At low fO_2, where competitive adsorption by O is limited, S typically enriches the interface ($\Gamma_S^{(Fe)} > 0$), so higher fS_2 promotes wetting. At higher fO_2 (roughly > IW), competitive adsorption by O can deplete S from the interface ($\Gamma_S^{(Fe)} < 0$), so further increases in fS_2 no longer reduce θ and may instead increase it.

Our experiments are consistent with this predicted reversal. With an FeO content of 20 wt% in olivine, where fO_2 is high and O coverage at the interface is large, FeS melts have higher θ (~50-56°) than eutectic melts (~42-52°), whereas at lower FeO (~5 wt%, lower fO_2), θ values are similar (~64-71°) for both melt compositions (Fig. 7**A-B**). This finding indicates that the sign and magnitude of $\Gamma_S^{(Fe)}$ change with fO_2 and FeO content, affecting the relative importance of fS_2 in controlling θ for eutectic and FeS melts.

By conducting experiments across a range of fO_2 and olivine FeO contents that span large variations in O solubility in sulfide melts, we directly assess the effect of the anion-to-cation ratio (S + O)/Fe on θ and interfacial energies (**Fig. S6**). Our data show a clear inverse correlation between θ and (S + O)/Fe, supporting the interpretation that S and O act together as surface-active species that reduce interfacial energies (Ballhaus and Ellis, 1996; Minarik et al., 1996; Gaetani and Grove, 1999). While Terasaki et al. (2008, 2005) also recognized a similar compositional trend between S and O, they did not find a consistent θ-(S + O)/Fe relationship, likely because strong P-T effects on O solubility and interfacial energies in their high-pressure experiments obscured the underlying compositional dependence. In contrast, Minarik et al. (1996) reported decreasing θ with increasing (S + O)/Fe at 3.5–4 GPa, and Gaetani and Grove (1999) documented the same trend at ambient pressure. Taken together with our results, these studies support the ability of S and O to lower interfacial energies, and thus θ, across a wide range of pressures.

The interconnection threshold ($\theta < 60°$) in eutectic melts is reached at ~10 wt% FeO, corresponding to fO_2 > IW+1 (Fig. 7**A**), consistent with observations at ambient pressure (Rose and Brenan, 2001). This

result implies that in oxidized planetesimals, eutectic Fe-O-S melts would form interconnected networks over a wide range of olivine FeO (≥10 wt%) even at low melt fractions (<1 vol%). For FeS melts, the interconnection threshold is reached only at higher FeO content in olivine (~15–19 wt%), i.e., ~5–10 wt% FeO higher than for eutectic melts (Fig. 7**B**). Previous FeS-melt studies (Minarik et al., 1996; Terasaki et al., 2005) reported systematically higher θ values for FeS-rich compositions, consistent with reduced O solubility at high pressures. Our results show that at the lower pressures and higher FeO contents characteristic of many oxidized planetesimals, FeS melts can nonetheless achieve $\theta < 60^\circ$ and undergo percolation.

A notable feature of our experimental data is that θ continues to decrease above ~ 10 wt% FeO (>IW+1), even though O content and (S + O)/Fe of eutectic melts increase only modestly and approach structural saturation (Fig. 7**A,** Fig. 9). This finding indicates that factors other than melt anion content also influence interfacial energies in this high-FeO, oxide-saturated regime. Once fO_2 >IW+2, an FeO-rich oxide precipitates at the silicate-melt interface and likely thickens with increasing fO_2 (Fig. 8**,** Fig. 2**O**). Simultaneously, the olivine itself becomes progressively more fayalitic, causing its composition to approach that of the interfacial FeO phase. This increasing chemical similarity between olivine and the FeO layer may reduce the olivine-melt interfacial energy and thus θ, even at nearly constant melt composition. We therefore suggest that the continued decrease in θ at high FeO reflects the combined effect of high melt anion contents and the FeO-rich oxides at the interface. This hypothesis could be tested by measuring interfacial energies directly in oxide-saturated systems.

We note that at the highest FeO contents, where an FeO-rich layer forms at the olivine-melt interface, the interpretation of dihedral angle measurements requires additional caution. The presence of a reaction product at the interface could, in principle, modify the geometry of the grain-boundary junction. However, the dihedral angles measured in these high-fO_2 experiments follow a continuous trend with the lower-fO_2 data (Fig. 7**A**), suggesting that the FeO layer does not fundamentally alter the wetting geometry. Nevertheless, dihedral angle values at the most oxidized conditions (fO_2 > IW+2) should be considered with greater uncertainty.

4.1.4. *Pressure control on O solubility and the Fe-O-S phase diagram*

Previous studies (Urakawa et al., 1987; Terasaki et al., 2008) have shown that pressure influences both O solubility in Fe-O-S melts and θ between metallic and silicate phases. Our experiments, combined with ambient-pressure data (Gaetani and Grove, 1999; Rose and Brenan, 2001), enable us to quantify this effect over a broad low-pressure range applicable to planetesimal core formation. Within 0–2 GPa, O solubility and θ are essentially insensitive to pressure at a given FeO content in the coexisting olivine **(**Fig. 5**C-D,** Fig. 7**C-D)**. Eutectic and FeS melts at 0.5, 1, and 2 GPa display similar O contents and dihedral angles for a given olivine FeO content, indicating that the dominant control on O solubility and wetting behavior in this regime is bulk composition (particularly, the FeO content in olivine), rather than pressure. These observations are consistent with measurements by Terasaki et al. (2008), who reported high O solubilities (~8–9 wt%) at 1.5 GPa, and with other low-pressure studies that document similarly elevated O solubilities in Fe-O-S melts (Naldrett, 1969; Gaetani and Grove, 1999; Rose and Brenan, 2001; Fonseca et al., 2008).

At higher pressures (P > 3 GPa), Terasaki et al. (2008) observed a marked decrease in O solubility, consistent with phase diagram studies of the Fe-O-S system (Urakawa et al., 1987). This decrease reflects pressure-induced changes in Fe-O-S phase relations: (1) the eutectic composition shifts from the FeO-FeS join at low pressure (<3 GPa) toward the Fe-FeS side at higher pressure, and (2) in the Fe-wüstite system the minimum melting point moves from the FeO side to the Fe side at ~3.3 GPa, causing the cotectic line linking the eutectic to rotate from the FeO-FeS side toward Fe-FeS. Experiments by Urakawa et al. (1987), when compared with low P data from Naldrett (1969), clearly document this shift between 1 bar and 6 GPa. The net effect is that increasing pressure above ~3–3.3 GPa shifts the equilibrium phase relations such that metallic melts accommodate less dissolved O.

This pressure dependence of O solubility is mirrored in θ. In our 0.5–2 GPa experiments, θ does not change systematically with pressure at fixed FeO, consistent with nearly constant O solubility across this range. By contrast, at P > 3 GPa, Terasaki et al. (2008) reported a significant increase in θ, coincident with their observed drop in O solubility (Fig. 7**C**). Together, these results show that pressure has little effect on O solubility and θ at low pressures, whereas at higher pressures (>3 GPa) phase-diagram changes in the Fe-O-S system strongly suppress O solubility and increase θ.

4.2. *Relevance to differentiation of oxidized chondritic bodies*

Oxidized chondritic bodies are prime candidates for planetesimals that underwent early episodes of core formation via percolation. To evaluate whether such bodies could plausibly form metallic cores by percolation, we first examine their redox states (fO_2) as inferred from bulk compositions of four representative chondrite groups: CV-ox, CM, CI, and RC (Fig. 1). RC chondrites formed in the inner Solar System reservoir, whereas CV-ox, CM, and CI chondrites originated in the outer Solar System reservoir (Fig. 1). We use their bulk compositions and redox states, together with our experimental constraints on O solubility and wetting behavior, to assess the viability and consequences of percolative core formation.

The bulk compositions of chondrites reported by Jarosewich (2006) include H_2O and C in addition to their oxide and metal components. These labile phases reside primarily in phyllosilicates and organics, which are thermally unstable and break down before core-mantle differentiation. Stoichiometric analysis shows that even in volatile-rich CI and CM chondrites, the H_2O budget exceeds organic C by a factor of ~1.4, ensuring that C is fully oxidized before metal-silicate segregation, while the excess H_2O cannot drive silicate Fe beyond the valence state already imposed by the oxide assemblage (see **Supplementary Text S2** for details). This interpretation is supported by the observed depletion of C, N, and H_2O in primitive achondrites and NC/CC iron meteorite parent bodies (Grewal et al., 2021c, 2022a, 2022b, 2025a; Grewal, 2022; Grewal and Asimow, 2023; Newcombe et al., 2023; Peterson et al., 2023, 2024; Grewal and Mukhopadhyay, 2025), as well as thermal evolution models showing efficient volatile removal during early metamorphism while interiors remain permeable (Lichtenberg et al., 2019). We therefore remove H_2O and C from the bulk compositions and renormalize the remaining oxides + metal to 100 wt% before calculating fO_2 and modeling core compositions.

In the Jarosewich (2006) compositions, total iron is reported as FeO, Fe_2O_3, and metallic Fe. For our fO_2 calculations, we recalculated all Fe_2O_3 as FeO equivalent, assuming all silicate iron is Fe^{2+}, and applied $\Delta IW = 2\log(X_{FeO}/X_{Fe})$. Using the renormalized chondrite compositions, we estimate fO_2 for each group (Fig. 1, Table 3). CI, CM, and RC chondrites are the most oxidized, with fO_2 typically near or above IW+2, and CV-ox chondrites are somewhat less oxidized (fO_2 ~IW+1.3). Our fO_2 estimates differ slightly from those of Bercovici et al. (2022) because we explicitly remove H_2O and C before computing Fe redox, in order to represent the residue that participates in core-mantle differentiation. However, the relative ordering of chondrite groups in fO_2 space is unchanged.

Our experimental results indicate that percolation of eutectic melts is viable in oxidized chondrite-like parent bodies once fO_2 approaches ~IW+1 (Fig. 8). At these conditions, θ falls below 60°, allowing metallic melt to form continuous networks at very low melt fractions. Typical oxidized chondrites have FeO contents above 20 wt% in their silicates **(**Table 3**)**, so this criterion is also satisfied for FeS melts. These observations imply that CV-ox, CM, CI, RC-like parent bodies could sustain interconnected Fe-O-S melt networks and, thus, percolative core formation without substantial silicate melting. We emphasize that

Table 3
Average bulk compositions of all oxidized chondritic groups, with errors representing 1σ standard deviation. Compositions were derived from previous studies. Core compositions were calculated based on the method described in **Section 4.2**.

Chondrite Type	FeO content (wt%)	Fe (wt%)	Ni (wt%)	FeS (wt%)		Core composition		
					ΔIW[1]	Fe + Ni (wt%)	S (wt%)	O (wt%)
CV-ox	27.56 (0.20)	0.16 (0.01)	0.30 (0.10)	4.16 (0.06)	1.27 (0.28)	63.8 (0.5)[2]	31.4 (1.6)	4.8 (1.5)
CM	27.51 (4.28)	0.08 (0.07)	0.32 (0.63)	8.41 (1.63)	2.43 (0.73)	63.8 (0.5)	32.6 (1.1)	3.6 (1.0)
CI	24.32 (na)	0.00[3] (na)	0.00 (na)	13.13 (na)	3.18 (na)	63.8 (0.5)	32.6 (1.1)	3.6 (1.0)
RC	29.43 (3.36)	0.20 (0.22)	0.95 (0.25)	7.83 (2.18)	2.04 (0.64)	63.8 (0.5)	29.8 (1.7)	6.4 (1.6)

1. The oxidation state relative to the iron-wüstite (IW) buffer is estimated via the equation: $\Delta IW = 2\log_{10}\left(\frac{X_{FeO}^{silicate}}{X_{Fe}^{metal}}\right)$, where $X_{FeO}^{silicate}$ and X_{Fe}^{metal} are the mole fractions of FeO in silicates and Fe in the metallic phase, respectively. We assume ideal behavior for both Fe and FeO ($\gamma_{Fe}^{metal} = 1$ and $\gamma_{FeO}^{silicate} = 1$), which provides a first-order estimate of fO_2.
2. The error margins for (Fe + Ni) were obtained from experimental data. For O, the errors are calculated from the best fit equations, and S errors are calculated as $\sigma_S = \sqrt{\sigma_O^2 + \sigma_{Fe}^2}$.
3. Because CI chondrites lack metallic Fe, an Fe metal content of 0.1 wt% is assumed for the purpose of calculating fO_2 and core composition modeling.

percolative core formation is a progressive process, not a single-temperature event. At the Fe-FeS eutectic (~988 °C; Buono and Walker, 2011), the initial melt constitutes ~1.8–5.1 wt% of the bulk rock, depending on the available metallic Fe (Table 3). However, with continued ^{26}Al-driven heating, remaining solid FeS progressively melts, and by ~1194 °C – the FeS liquidus – the entire metal + sulfide budget (4.6–13.1 wt%; Table 3) is liquid. Each increment of new melt satisfies the percolation criterion ($\theta < 60°$) at the FeO contents characteristic of these chondrites (>20 wt%; Table 3), so the core grows continuously as temperature rises. For CV-ox and RC bodies, where metallic Fe is present, eutectic melting at 988 °C already extracts ~38–50% of the total metal + sulfide budget on a molar basis, with the remainder melting progressively and well below the silicate solidus (~1050–1200 °C; Collinet and Grove, 2020a, 2020b). For CM and CI bodies, which lack metallic Fe, melting begins near the FeS liquidus (~1194 °C), coinciding with the onset of silicate partial melting. However, at these temperatures the silicate melt fraction remains small, and the olivine-dominated matrix retains its structural integrity – far below the rheological breakdown threshold (~30–40 vol% melt) and still below the silicate liquidus. Percolative metal segregation therefore remains viable in these bodies without requiring a magma ocean.

Having established that percolative core formation is viable across these chondrite groups, we now use our experimental constraints on wetting behavior and O solubility to predict the compositions of the resulting cores. As shown in **Section 4.1.3**, both O solubility and θ show limited variations over the range of 0–2 GPa at fixed FeO content, indicating that pressure has only a minor effect on melt connectivity in the low-pressure regime characteristic of planetesimal interiors. Fe-FeS eutectic melting in planetesimals is expected to begin at ~988 °C (Buono and Walker, 2011), whereas our experiments were conducted at 1350 °C to accelerate diffusion and ensure textural and chemical equilibrium between olivine and Fe-O-S melts within feasible run durations. The temperature dependence of O solubility in Fe-O-S melts is not well constrained: some studies report only modest changes with T (Fonseca et al., 2008), while other results suggest that O solubility might increase with T (Ueda et al., 2008; Pommier et al., 2018). Applying our 1350 °C results to planetesimal core formation at ~980–1200 °C therefore represents a first-order prediction of O solubility in Fe-O-S melts of oxidized planetesimals.

While fO_2 controls the range over which percolation is feasible, the mineralogy of the metallic phase determines the composition of the resulting core. Metallic phases in oxidized chondrites show compositional heterogeneity: CV-ox and RC contain intermediate amounts of metal and FeS, while CM/CI chondrites sample metal-poor, FeS-dominated bodies (Jarosewich, 2006; Bischoff et al., 2011). From CV-ox to CM/CI, the abundance of metallic Fe decreases while FeS increases. This systematic variation necessitates a compositional model that explicitly accounts for the specific composition of metallic phases. While previous models (e.g., Bercovici et al., 2022) predicted S-rich cores without explicitly including O, our results demonstrate that O incorporation into eutectic and FeS melts is substantial and varies systematically with metal composition. We therefore model core compositions as mixtures of two redox-dependent endmembers – a eutectic melt and FeS-dominated melt, corresponding to the early and late stages of progressive melting, respectively – which are represented by our eutectic and FeS experiments, respectively.

To parameterize how the O content in Fe-O-S melt of the eutectic endmember varies with fO_2 at $fO_2 < IW+2$, we adopt the framework of Fonseca et al. (2008), who performed experiments at ambient pressure to study O solubility in S-rich matte as a function of fO_2, fS_2 and T. Following Fonseca et al. (2008), we express the O content of eutectic Fe-O-S melts as a function of fO_2, by fitting the O solubility data from our eutectic experiments (Fig. 9):

$$\log_{10}[O]_{melt} = -1.298 + \frac{7619}{T(K)} + 0.334 \log fO_2 - 0.149 \log fS_2 \quad (19)$$

where $[O]_{melt}$ is the O content in wt%. The sulfur fugacity is constrained at $\log fS_2 = -2.916$, obtained by minimizing residuals between the equation and our eutectic O data ($\chi_\nu^2 = 2.878$), with $T = 1623$ K (1350 °C). This parameterization is preferred over the thermodynamic model of Kress (1997, 2000, 2007) because it expresses O solubility explicitly as a function of fO_2, fS_2, and T, making it directly applicable to our predictions for O contents in the cores of oxidized planetesimals. In eutectic melts, uncertainties of ± 0.5 wt% in the Fe content and ± 1.5 wt % in the O content propagate to uncertainties of ± 1.6 wt% in the calculated S content.

In the highly oxidized regime ($fO_2 > IW+2$), the eutectic data are well described by a simpler empirical relation than Eq. (19):

$$\log_{10}[O]_{melt} = 0.064 \log fO_2 + 0.838 \ (\chi^2 = 0.002) \quad (20)$$

which captures the more gradual increase in O content at high fO_2. For modeling purposes, we apply Eq. (19) for $fO_2 < IW+2$ and Eq. (20) for $fO_2 \geq IW+2$, with a sharp transition between the two regimes. The Fe content in eutectic Fe-O-S melts remains approximately constant at 63.8 ± 0.5 wt% across this range, consistent with the ternary phase diagram (Fig. 6) and previous experimental studies (Kress, 1997; Fonseca et al., 2008; Terasaki et al., 2008). This near constancy allows the S concentration to be calculated by difference to 100. Note that uncertainties of ± 0.5 wt% in Fe and ± 1 wt% in O propagate to uncertainties of ± 1.1 wt % in calculated S.

In contrast, FeS-rich melts form during progressive melting in bodies where metallic Fe is scarce or exhausted, so that melting proceeds on the

FeS-rich side of the eutectic. Oxygen solubility in FeS-rich melts differs from that in eutectic melts because of competitive adsorption between S and O at the interface, which limits O incorporation (**Section 4.1.1**). Consequently, the Fonseca et al. (2008) parameterization for eutectic-like melts cannot be directly applied to FeS-dominated compositions. Instead, we describe O contents in FeS-rich melts using a linear fit to our experimental data:

$$[O]_{melt} = 0.214\ FeO - 0.668\ (\chi^2 = 2.617) \quad (21)$$

where $[O]_{melt}$ is the O content by wt% and FeO is the FeO content of the coexisting silicate in wt%.

FeO content in oxidized chondrites varies from ~24 wt% in CI chondrites to ~30 wt% in RC chondrites, with CM and CV-ox chondrites showing an intermediate FeO content (Table 3). Oxygen content in FeS-rich melts increases approximately linearly from ~0.5–1 wt% at ~5 wt % FeO to ~3–5 wt% at ~20 wt% FeO (Fig. 5**B**). We select an FeS-rich melt equilibrated with 20 wt% FeO olivine as the representative end-member for modeling core compositions. At these conditions, FeS-rich melts contain 3.6 ± 1.0 wt% O, 32.6 ± 1.1 wt% S, and 63.8 ± 0.5 wt % Fe, substantially different from eutectic compositions in both O and S contents. Although CI and CM silicates have FeO contents of ~24–28 wt %, extrapolating Eq. (21) to these higher values yields O contents of only ~4.5–5.3 wt%, which fall within the 1σ uncertainty of the 20 wt% FeO calibration point. This endmember is therefore a conservative but representative choice for all modeled bodies.

Modeling core compositions as mixtures of the two endmembers – eutectic and FeS melts – we predict distinct core compositions for each group (Table 3; Fig. 10). We define two regimes of core formation based on initial metal content:

(i) Fe-metal-bearing bodies (e.g., CV-ox, RC, CK): In CV-ox and RC chondrites, there is insufficient metallic Fe to maintain eutectic Fe-O-S composition (at ~988 °C) throughout melt percolation, and metallic Fe is largely exhausted after an initial phase of eutectic melting. Subsequent melting and percolation would then occur at higher T (~1200 °C) on the FeS-rich side of the eutectic. The segregating melt composition evolves progressively from eutectic toward the FeS endmember as temperature increases, and the bulk core composition reflects the integrated contribution of melts produced across this temperature range. Applying this two-endmember framework to CV-ox and RC bulk compositions yields cores composed of roughly similar proportions of the two melts (e.g., CV-ox: ~39% eutectic, ~61% FeS-rich and RC: ~49% eutectic, ~51% FeS-rich). Given their compositional similarity to CV-ox (Greenwood et al., 2010), CK chondrites are expected to have similar core compositions.

(ii) Fe-metal-free bodies (e.g., CM, CI): For bodies that are devoid of metallic Fe, we consider that core-forming melts start directly as FeS-rich melts at T ~1194 °C. In this case, the segregating melt and the core would be dominated by an FeS-rich endmember. Given the lower O solubility we measured in FeS melts compared to eutectic melts, our models predict that CM and CI cores (~3.6 ± 1.0 wt% O) would be comparatively O-poor.

The systematic variation in core O content, from 6.4 wt% in RC to ~3.6 wt% in CM/CI (Fig. 10**A**), results from three effects: (1) the intrinsic decrease in O solubility from eutectic (7–10 wt% at fO_2 ~IW+2) to FeS-rich (~3–5 wt% at 20 wt% olivine FeO (fO_2 ~IW+2)) compositions, (2) the shifting mixing ratio from eutectic-dominated to FeS-dominated cores along the RC to CV-ox to CM/CI sequence, and (3) variations in fO_2 among these chondritic mineral assemblages, which modulate O solubility. In contrast, the predicted Fe + Ni content remains nearly constant (63.2–64.4 wt%) across all groups because Fe content in Fe-O-S melts is largely independent of fO_2 and fS_2. These predictions assume Ni behaves similarly to Fe in terms of partitioning and activity – an assumption that warrants future investigation but provides a first-order predictive framework for compositions of oxidized planetesimal cores.

The compositional differences we predict among RC, CV-ox, CM and CI chondrites are expressed primarily in their O and S contents, and these chemical variations can have implications for both the density of core-forming liquids and the possibility of liquid immiscibility. Density measurements by Kaiura and Toguri (1979) show that Fe-O-S melts have densities of ~3800 kg/m^3 at high T (~1200–1350 °C) – only slightly lower than those of FeS melts (~3800–3900 kg/m^3), implying that the addition of a few wt% O does not strongly affect core densities. In

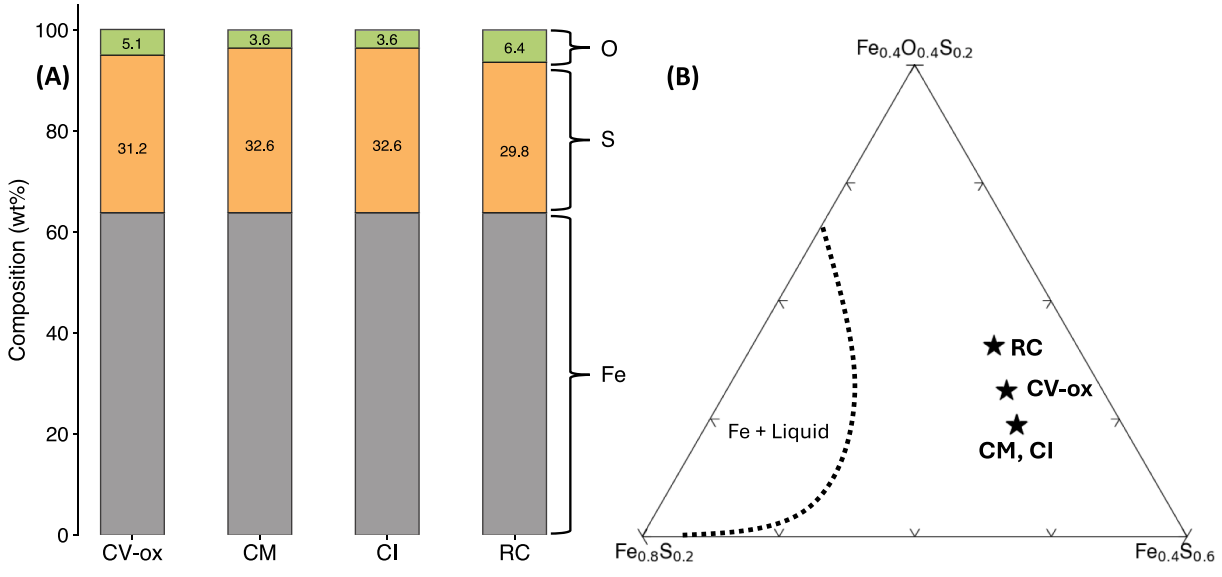

Fig. 10. (A) Stacked columns illustrating the average core compositions of the parent bodies of oxidized carbonaceous chondrites and RC chondrites upon differentiation. The modelled compositions are a combination of eutectic melts and FeS-rich melts. The columns in the grey, orange and green bars represent the Fe, S and O concentrations by wt%, respectively. Core compositions in CK chondrites are expected to be similar to those of CV-ox owing to their similar bulk compositions. (B) Fe-O-S ternary diagram showing the core compositions for cores of RC, CV-ox, CM and CI-like bodies. Dotted line shows the phase boundary in the Fe-O-S system at 1400 °C as determined by Kress (1997).

composition space, the Fe-O-S phase diagram is characterized by a very large immiscibility gap that produces two coexisting metallic melts: an O-rich, S-rich, Fe-poor melt, and an O-poor, S-poor, Fe-rich melt (Kress, 1997; Tsuno et al., 2007; Chabot et al., 2015; Pommier et al., 2018). The highly oxidized planetesimals considered in this study fall outside this immiscibility field during core formation (Fig. 10**B**), but bodies with lower fO_2 and fS_2 could produce immiscible liquids, leading to the formation of a Fe-rich inner core and a Fe-poor outer core that is enriched in both S and O.

4.3. Limitations and Uncertainties in Core Composition Predictions

4.3.1. Ni effects on O solubility in metallic melts

Our core composition calculations assume that Ni and Fe behave identically during melt percolation. In reality, oxidized chondrites contain substantial Ni in their metal phases (5–15 wt%; Kimura et al., 2011), and multiple experimental studies hint that Ni exerts a measurable influence on O solubility in metallic melts (Gaetani and Grove, 1999; Rose and Brenan, 2001; Kress, 2007; Fonseca et al., 2008). According to Kress (2007), at fixed fO_2, Ni systematically reduces O solubility in Fe-Ni-O-S melts, though the exact magnitude depends on Ni concentration, fO_2, and T. Consequently, our estimated O contents in the cores based on Fe-O-S systematics should be regarded as first-order predictions. This effect is most consequential for CM and CI cores, where the predicted O content of ~3.6 wt% represents the smallest enrichment among the modeled groups and is therefore most sensitive to downward revision because of the effect of Ni. Quantifying this correction remains an important target for future Ni-bearing experiments at oxidizing conditions.

4.3.2. Pyroxene effects and silicate mineralogy

Although olivine is the dominant phase in chondritic silicate assemblages, pyroxene can be a significant secondary component: pyroxene/(pyroxene + olivine) reaches ~0.3 in CI and CM chondrites (Collinet and Grove, 2020a, 2020b). To fully constrain percolation behavior in these bodies, mixed olivine-pyroxene systems need to be investigated in future experiments. Recent observations by Miura et al. (2025) indicate that eutectic and FeS melts coexisting with orthopyroxene dissolve less O than those coexisting with olivine. This implies that our olivine-only experiments likely provide maximum estimates for O solubility in eutectic and FeS melts. The effects of pyroxene modal abundance, composition, and fO_2 on both O solubility and θ however remains poorly constrained, and dedicated mixed-mineralogy studies will be required to refine percolation and core-composition models for oxidized, pyroxene-bearing bodies.

5. Conclusion

This study investigates how O-bearing Fe-O-S metallic melts percolate through solid olivine aggregates, in order to constrain the efficacy of percolative core formation in oxidized bodies. Our experiments quantify the effects of olivine FeO content (and thus, fO_2), metallic melt composition, and pressure on O solubility and dihedral angles in Fe-O-S systems. Within the low-pressure (<2 GPa) regime relevant to planetesimal interiors, the metal connectivity and the composition of Fe-O-S melts are governed primarily by redox state (fO_2) and metallic melt composition, with pressure playing a comparatively minor role.

The key findings from our experiments are:

(1) Olivine FeO content, O solubility, and the onset of metallic melt connectivity: The FeO content of coexisting olivine, together with the Fe-rich eutectic vs. FeS-rich character of the metallic melt, controls both O solubility and dihedral angle (θ). Increasing olivine FeO increases O solubility and decreases θ. In eutectic melts, θ falls below the interconnection threshold ($\theta < 60°$) at ~10 wt% FeO, whereas FeS melts require ~15–19 wt% FeO to achieve connectivity. Under these conditions, Fe-O-S melts can form interconnected networks even at very low melt fractions (<1 vol%), with eutectic melts becoming percolative at lower olivine FeO contents than FeS melts. These results complement micro-CT studies showing high interconnection thresholds (~14 vol%) for O-poor Fe-S melts (Solferino et al., 2020). Our work demonstrates that O dissolution under oxidizing conditions shifts the system to a percolating regime at melt fractions well below 1 vol%.

(2) S and O as synergistic surface-active species: Across both eutectic and FeS compositions, the anion-to-cation ratio (S + O)/Fe inversely correlates with θ, indicating that both S and O act as surface-active elements that lower solid-melt interfacial energies and promote melt interconnectivity. A Langmuir-type competitive adsorption framework explains the differing O solubilities and θ-composition trends in eutectic versus FeS melts: at fixed fO_2 , a higher fS_2 increases interfacial S coverage and suppresses O solubility, whereas increasing fO_2 drives O onto interfacial sites at the expense of S.

(3) Limited pressure effects at planetesimal conditions: At pressures relevant to planetesimal interiors (<2 GPa), O solubility in Fe-O-S melts remains nearly constant, and dihedral angles show little variation. Only at pressures exceeding ~3 GPa does O solubility drop, and dihedral angles increase significantly. Thus, for planetesimal-like conditions, pressure is not a first-order control on metallic melt connectivity; instead, fO_2 and bulk composition dominate the wetting properties.

(4) Implications for oxidized chondritic bodies and core compositions: Modeling of oxidized chondritic bodies (RC, CV-ox, CK, CM, and CI) with our experimentally defined connectivity and O solubility thresholds indicates that their metallic melts would percolate to form cores before widespread silicate melting (silicate solidus ~1050–1200 °C; Collinet and Grove, 2020a, 2020b). Percolative core formation is a progressive process: with continued ^{26}Al-driven heating, the entire metal + sulfide budget (4.6–13.1 wt%) becomes liquid by ~1194 °C, and each increment of melt satisfies the percolation criterion at the FeO contents characteristic of these chondrites. Using a two-endmember framework reflecting progressive melting from eutectic to FeS-rich compositions, we predict the highest O contents (~6 wt% O) for RC-like bodies, lower O contents for CV-ox and CK (~5 wt% O), and O-poor cores (~3–4 wt% O) for CM/CI analogs. These O contents are first-order estimates; both the temperature offset between our experiments (1350 °C) and natural core formation (~988–1200 °C), and the effect of Ni on suppressing O solubility, indicate that actual core O contents may be somewhat lower.

CRediT authorship contribution statement

Varun Manilal: Writing – review & editing, Writing – original draft, Visualization, Validation, Software, Methodology, Investigation, Formal analysis, Data curation. **Kyusei Tsuno:** Writing – review & editing, Methodology. **Hideharu Kuwahara:** Writing – review & editing. **Axel Wittmann:** Writing – review & editing. **Anne Pommier:** Writing – review & editing. **Christy Till:** Resources. **Damanveer S. Grewal:** Writing – review & editing, Writing – original draft, Validation, Supervision, Resources, Project administration, Methodology, Funding acquisition, Conceptualization.

Declaration of competing interest

The authors declare that they have no known competing financial interests or personal relationships that could have appeared to influence the work reported in this paper.

Acknowledgements

We would like to thank Geoff Bromiley and two anonymous reviewers for their detailed comments that helped us significantly improve the clarity of our communication. A.E. Bernard Charlier is thanked for his efficient handling of the manuscript. This study was funded by startup funds from Yale University to D.S.G.

Appendix A. Supplementary material

The Supplementary Material associated with this article includes a step-by-step thermodynamic derivation of O solubility in Fe-O-S melts and its impact on dihedral angles. Additionally, a stoichiometric argument is outlined to justify the removal of water and carbon from the bulk chondritic compositions prior to calculating the modeled core compositions. The Supplementary Material also contains a data table with redox states of early Solar System planetesimals. Supplementary material to this article can be found online at https://doi.org/10.1016/j.gca.2026.06.018.

Data availability

Data are available through Mendeley Data at https://doi.org/10.17632/4zsnph29sy.1.

References

Ballhaus, C., Ellis, D.J., 1996. Mobility of core melts during Earth's accretion. Earth Planet. Sci. Lett. 143, 137–145.

Bennett, M.E.I., McSween Jr., H.Y., 1996. Revised model calculations for the thermal histories of ordinary chondrite parent bodies. Meteorit. Planet. Sci. 31, 783–792.

Bercovici, H.L., Elkins-Tanton, L.T., O'Rourke, J.G., Schaefer, L., 2022. The effects of bulk composition on planetesimal core sulfur content and size. Icarus 380, 114976.

Bischoff, A., Vogel, N., Roszjar, J., 2011. The Rumuruti chondrite group. Geochemistry 71, 101–133.

Biswas, J., Gu, K., Coley, K.S., 2022. Consideration of the competitive adsorption of oxygen and sulfur on the decarburization kinetics of Fe–C droplets in oxidizing slag. Metall. Mater. Trans. B 53, 4087–4104.

Bose, K., Ganguly, J., 1995. Quartz-coesite transition revisited; reversed experimental determination at 500-1200 degrees C and retrieved thermochemical properties. Am. Mineral. 80, 231–238.

Bromiley, G.D., 2023. The geochemical legacy of low-temperature, percolation-driven core formation in planetesimals. Earth Moon Planet. 127, 4.

Bruhn, D., Groebner, N., Kohlstedt, D.L., 2000. An interconnected network of core-forming melts produced by shear deformation. Nature 403, 883–886.

Bulau, J.R., Waff, H.S., Tyburczy, J.A., 1979. Mechanical and thermodynamic constraints on fluid distribution in partial melts. J. Geophys. Res. Solid Earth 84, 6102–6108.

Buono, A.S., Walker, D., 2011. The Fe-rich liquidus in the Fe–FeS system from 1 bar to 10 GPa. Geochim. Cosmochim. Acta 75, 2072–2087.

Cao, W., 2010. Theoretical and experimental studies of surface and interfacial phenomena involving steel surfaces. Skolan för industriell teknik och management, Kungliga Tekniska högskolan, Stockholm. Ph.D. thesis.

Chabot, N.L., Wollack, E.A., Humayun, M., Shank, E.M., 2015. The effect of oxygen as a light element in metallic liquids on partitioning behavior. Meteorit Planet Scien 50, 530–546.

Collinet, M., Grove, T.L., 2020a. Formation of primitive achondrites by partial melting of alkali-undepleted planetesimals in the inner solar system. Geochim. Cosmochim. Acta 277, 358–376.

Collinet, M., Grove, T.L., 2020b. Widespread production of silica- and alkali-rich melts at the onset of planetesimal melting. Geochim. Cosmochim. Acta 277, 334–357.

Crossley, S.D., Ash, R.D., Sunshine, J.M., Corrigan, C.M., McCoy, T.J., 2023. Parent body histories recorded in Rumuruti chondrite sulfides: Implications for the onset of oxidized, sulfur-rich core formation. Meteorit Planet Scien 58, 383–404.

Crossley, S.D., Setera, J.B., Anzures, B.A., Iacovino, K., Buckley, W.P., Eckley, S.A., O'Neal, E.W., Maisano, J.A., Simon, J.I., Righter, K., 2025. Percolative sulfide core formation in oxidized planetary bodies. Nat. Commun. 16, 3233.

Dunn, T.L., Cressey, G., McSween Jr, H.Y., McCoy, T.J., 2010. Analysis of ordinary chondrites using powder X-ray diffraction: 1. Modal mineral abundances. Meteorit. Planet. Sci. 45, 123–134.

Eustathopoulos, N., Nicholas, M.G., Drevet, B., 1999. Wettability at high temperatures, 1st ed. Pergamon materials series. Pergamon, Amsterdam New York.

Faul, U.H., 1997. Permeability of partially molten upper mantle rocks from experiments and percolation theory. J. Geophys. Res. Solid Earth 102, 10299–10311.

Fonseca, R.O.C., Campbell, I.H., O'Neill, H., St, C., Fitzgerald, J.D., 2008. Oxygen solubility and speciation in sulphide-rich mattes. Geochim. Cosmochim. Acta 72, 2619–2635.

Gaetani, G.A., Grove, T.L., 1999. Wetting of mantle olivine by sulfide melt: implications for Re/Os ratios in mantle peridotite and late-stage core formation. Earth Planet. Sci. Lett. 169, 147–163.

Ghanbarzadeh, S., Hesse, M.A., Prodanović, M., 2017. Percolative core formation in planetesimals enabled by hysteresis in metal connectivity. PNAS 114, 13406–13411.

Ghosh, A., McSween, H.Y., 1998. A thermal model for the differentiation of asteroid 4 vesta, based on radiogenic heating. Icarus 134, 187–206.

Goodrich, C.A., Ash, R.D., Van Orman, J.A., Domanik, K., McDonough, W.F., 2013. Metallic phases and siderophile elements in main group ureilites: Implications for ureilite petrogenesis. Geochim. Cosmochim. Acta 112, 340–373.

Greenwood, R.C., Franchi, I.A., Kearsley, A.T., Alard, O., 2010. The relationship between CK and CV chondrites. Geochim. Cosmochim. Acta 74, 1684–1705.

Grewal, D.S., 2022. Origin of nitrogen isotopic variations in the rocky bodies of the solar system. ApJ 937, 123.

Grewal, D.S., Asimow, P.D., 2023. Origin of the superchondritic carbon/nitrogen ratio of the bulk silicate Earth – an outlook from iron meteorites. Geochim. Cosmochim. Acta 344, 146–159.

Grewal, D.S., Bhattacharjee, S., Zhang, B., Nie, N.X., Miyazaki, Y., 2025a. Enrichment of moderately volatile elements in first-generation planetesimals of the inner Solar System. Sci. Adv. 11, eadq7848.

Grewal, D.S., Dasgupta, R., Aithala, S., 2021a. The effect of carbon concentration on its core-mantle partitioning behavior in inner Solar System rocky bodies. Earth Planet. Sci. Lett. 571, 117090.

Grewal, D.S., Dasgupta, R., Holmes, A.K., Costin, G., Li, Y., Tsuno, K., 2019a. The fate of nitrogen during core-mantle separation on Earth. Geochim. Cosmochim. Acta 251, 87–115.

Grewal, D.S., Dasgupta, R., Hough, T., Farnell, A., 2021b. Rates of protoplanetary accretion and differentiation set nitrogen budget of rocky planets. Nat. Geosci. 14, 369–376.

Grewal, D.S., Dasgupta, R., Marty, B., 2021c. A very early origin of isotopically distinct nitrogen in inner Solar System protoplanets. Nat. Astron 5, 356–364.

Grewal, D.S., Dasgupta, R., Sun, C., Tsuno, K., Costin, G., 2019b. Delivery of carbon, nitrogen, and sulfur to the silicate Earth by a giant impact. Sci. Adv. 5, eaau3669.

Grewal, D.S., Mukhopadhyay, S., 2025. Using carbon isotopes to trace the origin of volatiles on Earth and Mars. Geochim. Cosmochim. Acta 408, 12–27.

Grewal, D.S., Nie, N.X., Zhang, B., Izidoro, A., Asimow, P.D., 2024. Accretion of the earliest inner Solar System planetesimals beyond the water snowline. Nat. Astron 8, 290–297.

Grewal, D.S., Seales, J.D., Dasgupta, R., 2022a. Internal or external magma oceans in the earliest protoplanets – perspectives from nitrogen and carbon fractionation. Earth Planet. Sci. Lett. 598, 117847.

Grewal, D.S., Sun, T., Aithala, S., Hough, T., Dasgupta, R., Yeung, L.Y., Schauble, E.A., 2022b. Limited nitrogen isotopic fractionation during core-mantle differentiation in rocky protoplanets and planets. Geochim. Cosmochim. Acta 338, 347–364.

Grewal, D.S., Zhang, Z., Manilal, V., Kruijer, T.S., Bottke, W.F., Stewart, S.T., 2025b. Protracted core formation and impact disruptions shaped the earliest outer Solar System planetesimals. Sci. Adv. 11, eadw1668.

Helffrich, G., Kaneshima, S., 2004. Seismological constraints on core composition from Fe-O-S liquid immiscibility. Science 306, 2239–2242.

Hevey, P.J., Sanders, I.S., 2006. A model for planetesimal meltdown by 26Al and its implications for meteorite parent bodies. Meteorit. Planet. Sci. 41, 95–106.

Holness, M.B., Lewis, S., 1997. The structure of the halite-brine interface inferred from pressure and temperature variations of equilibrium dihedral angles in the halite-H2O CO2 system. Geochim. Cosmochim. Acta 61, 795–804.

Holzheid, A., Schmitz, M.D., Grove, T.L., 2000. Textural equilibria of iron sulfide liquids in partly molten silicate aggregates and their relevance to core formation scenarios. J. Geophys. Res. 105, 13555–13567.

Iacovino, K., 2021. Ferric/Ferrous, Fe3+/FeT, fO2 Converter (Kress and Carmichael, 1991) (3.2). Zenodo. https://doi.org/10.5281/zenodo.5907844.

Jarosewich, E., 2006. Chemical analyses of meteorites at the Smithsonian Institution: an update. Meteorit. Planet. Sci. 41, 1381–1382.

Kaiura, G.H., Toguri, J.M., 1979. Densities of the molten fes, Fes–Cu_2 S and Fe–S–O Systems—utilizing a bottom-balance archimedean technique. Can. Metall. Q. 18, 155–164.

Keil, K., Stöffler, D., Love, S.G., Scott, E.R.D., 1997. Constraints on the role of impact heating and melting in asteroids. Meteorit. Planet. Sci. 32, 349–363.

Kimura, M., Grossman, J.N., Weisberg, M.K., 2011. Fe-Ni metal and sulfide minerals in CM chondrites: an indicator for thermal history. Meteorit. Planet. Sci. 46, 431–442.

Kiseeva, E.S., Wood, B.J., 2013. A simple model for chalcophile element partitioning between sulphide and silicate liquids with geochemical applications. Earth Planet. Sci. Lett. 383, 68–81.

Kiseeva, E.S., Wood, B.J., 2015. The effects of composition and temperature on chalcophile and lithophile element partitioning into magmatic sulphides. Earth Planet. Sci. Lett. 424, 280–294.

Kress, V., 1997. Thermochemistry of sulfide liquids. I. the system O-S-Fe at 1 bar. Contrib. Miner. Petrol. 127, 176–186.

Kress, V., 2000. Thermochemistry of sulfide liquids. II. Associated solution model for sulfide liquids in the system O-S-Fe. Contrib. Miner. Petrol. 139, 316–325.

Kress, V., 2007. Thermochemistry of sulfide liquids III: Ni-bearing liquids at 1 bar. Contrib. Miner. Petrol. 154, 191–204.

Kruijer, T.S., Touboul, M., Fischer-Gödde, M., Bermingham, K.R., Walker, R.J., Kleine, T., 2014. Protracted core formation and rapid accretion of protoplanets. Science 344, 1150–1154.

Langmuir, I., 1918. The adsorption of gases on plane surfaces of glass, mica and platinum. J. Am. Chem. Soc. 40, 1361–1403.

Laporte, D., Provost, A., 2000. The Grain-Scale distribution of Silicate, Carbonate and Metallosulfide Partial Melts: a Review of Theory and Experiments. In: Bagdassarov, N., Laporte, D., Thompson, A.B. (Eds.), Physics and Chemistry of Partially Molten Rocks. Springer, Netherlands, Dordrecht, pp. 93–140.

Lasaga, A.C., 2014. Kinetic Theory in the Earth Sciences. Princeton University Press, Princeton.

Liang, L.-C., 1991. Study of oxygen peak shifts among some minerals using a tungsten–silicon multilayer pseudo-crystal. X-Ray Spectrom. 20, 89–90.

Lichtenberg, T., Golabek, G.J., Burn, R., Meyer, M.R., Alibert, Y., Gerya, T.V., Mordasini, C., 2019. A water budget dichotomy of rocky protoplanets from 26Al-heating. Nat. Astron 3, 307–313.

McCoy, T.J., Carlson, W.D., Nittler, L.R., Stroud, R.M., Bogard, D.D., Garrison, D.H., 2006. Graves Nunataks 95209: a snapshot of metal segregation and core formation. Geochim. Cosmochim. Acta 70, 516–531.
Médard, E., Grove, T.L., 2006. Early hydrous melting and degassing of the Martian interior. J. Geophys. Res. Planets 111.
Medard, E., McCammon, C.A., Barr, J.A., Grove, T.L., 2008. Oxygen fugacity, temperature reproducibility, and H2O contents of nominally anhydrous piston-cylinder experiments using graphite capsules. Am. Mineral. 93, 1838–1844.
Merk, R., Breuer, D., Spohn, T., 2002. Numerical modeling of 26Al-induced radioactive melting of asteroids considering accretion. Icarus 159, 183–191.
Minarik, W.G., Ryerson, F.J., Watson, E.B., 1996. Textural entrapment of core-forming melts. Science 272, 530–533.
Miura, T., Terasaki, H., Takaki, H., Kobayashi, K., Bromiley, G.D., Yoshino, T., 2025. The effect of pressure on dihedral angle between liquid Fe-S and orthopyroxene: Implication for percolative core formation in planetesimals and planetary embryos. Meteorit. Planet. Sci. 60, 2811–2827.
Monnereau, M., Guignard, J., Néri, A., Toplis, M.J., Quitté, G., 2023. Differentiation time scales of small rocky bodies. Icarus 390, 115294.
Moskovitz, N., Gaidos, E., 2011. Differentiation of planetesimals and the thermal consequences of melt migration. Meteorit. Planet. Sci. 46, 903–918.
Naldrett, A.J., 1969. A portion of the system Fe–S–O between 900 and 1080 °C and its application to sulfide ore magmas. J Petrology 10, 171–201.
Néri, A., Guignard, J., Monnereau, M., Toplis, M.J., Quitté, G., 2019. Metal segregation in planetesimals: Constraints from experimentally determined interfacial energies. Earth Planet. Sci. Lett. 518, 40–52.
Neumann, W., Breuer, D., Spohn, T., 2012. Differentiation and core formation in accreting planetesimals. A&A 543, A141.
Newcombe, M.E., Nielsen, S.G., Peterson, L.D., Wang, J., Alexander, C.M.O., Sarafian, A. R., Shimizu, K., Nittler, L.R., Irving, A.J., 2023. Degassing of early-formed planetesimals restricted water delivery to Earth. Nature 615, 854–857.
Nichols, S.J., Mackwell, S.J., 1991. Grain growth in porous olivine aggregates. Phys Chem Minerals 18.
Peterson, L.D., Newcombe, M.E., Alexander, C.M.O., Wang, J., Klein, F., Bekaert, D.V., Nielsen, S.G., 2023. The H content of aubrites: an evaluation of bulk versus in situ methods for quantifying water in meteorites. Earth Planet. Sci. Lett. 620, 118341.
Peterson, L.D., Newcombe, M.E., Alexander, C.M.O., Wang, J., Nielsen, S.G., 2024. The H-poor nature of incompletely melted planetesimals: the view from acapulcoites and lodranites. Geochim. Cosmochim. Acta 370, 1–14.
Pommier, A., Laurenz, V., Davies, C.J., Frost, D.J., 2018. Melting phase relations in the Fe-S and Fe-S-O systems at core conditions in small terrestrial bodies. Icarus 306, 150–162.
Qi, C., Zhao, Y.-H., Zimmerman, M.E., Kim, D., Kohlstedt, D.L., 2021. Evolution of Microstructural Properties in Sheared Iron-Rich Olivine. J. Geophys. Res. Solid Earth 126, e2020JB019629.
Righter, K., Sutton, S.R., Danielson, L., Pando, K., Newville, M., 2016. Redox variations in the inner solar system with new constraints from vanadium XANES in spinels. Am. Mineral. 101, 1928–1942.
Roberts, J.J., Kinney, J.H., Siebert, J., Ryerson, F.J., 2007. Fe-Ni-S melt permeability in olivine: Implications for planetary core formation. Geophys. Res. Lett. 34.
Rose, L.A., Brenan, J.M., 2001. Wetting properties of Fe-Ni-Co-Cu-O-S melts against olivine: implications for sulfide melt mobility. Econ. Geol. 96, 145–157.
Sahijpal, S., Ivanova, M.A., Kashkarov, L.L., Korotkova, N.N., Migdisova, L.F., Nazarov, M.A., Goswami, J.N., 1995. 26Al as a heat source for early melting of planetesimals: results from isotopic studies of meteorites. Proc. Indian Acad. Sci. - Earth Planet. Sci. 104, 555–567.
Sahijpal, S., Soni, P., Gupta, G., 2007. Numerical simulations of the differentiation of accreting planetesimals with 26Al and 60Fe as the heat sources. Meteorit. Planet. Sci. 42, 1529–1548.
Shannon, M.C., Agee, C.B., 1996. High pressure constraints on percolative core formation. Geophys. Res. Lett. 23, 2717–2720.
Solferino, G.F.D., Golabek, G.J., 2018. Olivine grain growth in partially molten Fe–Ni–S: a proxy for the genesis of pallasite meteorites. Earth Planet. Sci. Lett. 504, 38–52.
Solferino, G.F.D., Thomson, P.-R., Hier-Majumder, S., 2020. Pore Network Modeling of Core Forming Melts in Planetesimals. Front. Earth Sci. 8.
Stevenson, D.J., 1988. Fluid Dynamics of Core Formation. In: Presented at the Topical Conference Origin of the Earth, p. 87.
Tauber, M.J., Saxena, S., Bullock, E.S., Ginestet, H., Pommier, A., 2023. Electrical properties of iron sulfide-bearing dunite under pressure: effect of temperature, composition, and annealing time. Am. Mineral. 108, 2193–2208.
Terasaki, H., Frost, D.J., Rubie, D.C., Langenhorst, F., 2005. The effect of oxygen and sulphur on the dihedral angle between Fe–O–S melt and silicate minerals at high pressure: Implications for Martian core formation. Earth Planet. Sci. Lett. 232, 379–392.
Terasaki, H., Frost, D.J., Rubie, D.C., Langenhorst, F., 2008. Percolative core formation in planetesimals. Earth Planet. Sci. Lett. 273, 132–137.
Tonks, W.B., Melosh, H.J., 1992. Core formation by giant impacts. Icarus 100, 326–346.
Tsuno, K., Grewal, D.S., Dasgupta, R., 2018. Core-mantle fractionation of carbon in Earth and Mars: the effects of sulfur. Geochim. Cosmochim. Acta 238, 477–495.
Tsuno, K., Grewal, D.S., Xu, V., Leinbach, L., Leinenweber, K., Wittmann, A., Shim, S.-H., 2024. The effect of Nitrogen on the Dihedral Angle between Fe−Ni Melt and Ringwoodite: Implications for the Nitrogen Deficit in the Bulk Silicate Earth. Geophys. Res. Lett. 51, e2024GL109584.
Tsuno, K., Terasaki, H., Ohtani, E., Suzuki, A., Asahara, Y., Nishida, K., Sakamaki, T., Funakoshi, K., Kikegawa, T., 2007. In situ observation and determination of liquid immiscibility in the Fe-O-S melt at 3 GPa using a synchrotron X-ray radiographic technique. Geophys. Res. Lett. 34, 2007GL030750.
Ueda, S., Yamaguchi, K., Takeda, Y., 2008. Phase equilibrium and activities of Fe-S-O melts. Mater. Trans. 49, 572–578.
Urakawa, S., Kato, M., Kumazawa, M., 1987. Experimental study on the phase relations in the system Fe-Ni-O-S up to 15 GPa. In: Manghnani, M.H., Syono, Y. (Eds.), Geophysical Monograph Series. American Geophysical Union, Washington, D. C., pp. 95–111
Urey, H.C., 1955. The cosmic abundances of potassium, uranium, and thorium and the heat balances of the earth, the moon, and mars*. Proc. Natl. Acad. Sci. 41, 127–144.
von Bargen, N., Waff, H.S., 1986. Permeabilities, interfacial areas and curvatures of partially molten systems: results of numerical computations of equilibrium microstructures. J. Geophys. Res. Solid Earth 91, 9261–9276.
Waff, H.S., Faul, U.H., 1992. Effects of crystalline anisotropy on fluid distribution in ultramafic partial melts. J. Geophys. Res. 97, 9003–9014.
Walker, R.M., Cameron, A.G.W., 2006. Meteorites and the Early Solar System II. University of Arizona Press, Tucson.
Walte, N.P., Rubie, D.C., Bons, P.D., Frost, D.J., 2011. Deformation of a crystalline aggregate with a small percentage of high-dihedral-angle liquid: Implications for core–mantle differentiation during planetary formation. Earth Planet. Sci. Lett. 305, 124–134.
Yoshino, T., Walter, M.J., Katsura, T., 2003. Core formation in planetesimals triggered by permeable flow. Nature 422, 154–157.
Yoshino, T., Walter, M.J., Katsura, T., 2004. Connectivity of molten Fe alloy in peridotite based on in situ electrical conductivity measurements: implications for core formation in terrestrial planets. Earth Planet. Sci. Lett. 222, 625–643.
Zhao, Y.-H., Zimmerman, M.E., Kohlstedt, D.L., 2009. Effect of iron content on the creep behavior of olivine: 1. Anhydrous conditions. Earth Planet. Sci. Lett. 287, 229–240.